Multidimensional Modeling of Type I X-ray Bursts. I. Two-Dimensional Convection Prior to the Outburst

C. M. Malone[1], A. Nonaka[2], A. S. Almgren[2], J. B. Bell[2], M. Zingale[1]

ABSTRACT

The surface explosion which occurs in a Type I X-ray burst (XRB) is strongly influenced by the underlying neutron star's parameters such as mass, radius and rotational frequency making XRBs interesting tools to help constrain the equation of state of dense matter. A complete theoretical understanding of the bursting phenomenon including the ignition and propagation of the subsonic burning front will instruct us *how* to use such tools. In the past, it has been computationally difficult to model XRBs in multiple dimensions because of the low Mach number flow and the large range in physical scales of the system. We present results of the early convective phase preceding ignition of an XRB using the low Mach number approximation code, `MAESTRO`. We find the resolution requirements to accurately model the thin burning layer to be an order of magnitude higher than previously used in the literature. We furthermore explore the strong effects convection has on regulating the state of the material in which the burning front will eventually propagate.

Subject headings: convection — hydrodynamics — methods: numerical — stars: neutron — X-rays: bursts

1. Introduction

Given that they are possibly the most frequent thermonuclear explosions in the universe, Type I X-ray Bursts (hereafter XRBs) provide an excellent testbed for determining the properties of matter near the surface of a neutron star. To make meaningful inferences about these properties from observational data, however, we must have a proper theoretical understanding of the bursting phenomena (Bhattacharyya 2010). The basic XRB paradigm

[1]Dept. of Physics & Astronomy, Stony Brook University, Stony Brook, NY 11794-3800

[2]Center for Computational Science and Engineering, Lawrence Berkeley National Laboratory, Berkeley, CA 94720

takes place in a mass transferring, low-mass X-ray binary (LMXB) system in which the neutron star's companion has filled its Roche lobe and is dumping H- and/or He-rich material onto the surface of the neutron star. Depending on the accretion rate and composition, there are several burning regimes which will trigger an XRB (see Bildsten 2000, for an overview). The general idea is that a column of accreted material, or heavier-element ash from prior stable burning of accreted material, builds up until the temperature sensitivity of the energy generation rate at the base of the layer exceeds that of the local cooling rate and a thin-shell thermal instability forms. The instability eventually causes a runaway of unstable burning resulting in an outburst.

One-dimensional hydrodynamic studies have been able to reproduce many of the observable features of XRBs such as burst energies ($\sim 10^{39}$ erg), rise times (seconds), durations (10's – 100's of seconds) and recurrence times (hours to days) (Woosley & Weaver 1984; Taam et al. 1993; Heger et al. 2007; also see Strohmayer & Bildsten 2006, for a review of XRBs). By construction, however, one-dimensional models assume that the fuel is burned uniformly over the surface of the star which is unlikely if the accretion is not spherically symmetric (Shara 1982). Furthermore, the *Rossi X-ray Timing Explorer* satellite has observed coherent oscillations in the lightcurves of ~ 20 outbursts from LMXB systems (first by Strohmayer et al. 1996; more recently by Altamirano et al. 2010 and references therein). The asymptotic evolution of the frequency of such oscillations suggests they are modulated by the neutron star spin frequency (Muno et al. 2002). Oscillations observed during the rising portion of an outburst lightcurve are therefore indicative of a spreading burning front being brought in and out of view by stellar rotation. Additionally, oscillations observed during the decay phase of the burst are thought to be caused by unstable surface modes which may depend critically on the local heating and cooling rates during the burst (Narayan & Cooper 2007, and references therein). The manner in which the burning front spreads and propagates throughout the accreted atmosphere is not well known, and a proper modeling of the conditions in the atmosphere prior to outburst is needed. These phenomena are inherently multidimensional.

Prior to the actual outburst, the burning at the base of the ignition column will drive convection throughout the overlying layers and set the state of the material in which the burning front will propagate. One-dimensional simulations of XRBs usually attempt to parameterize the convective overturn and mixing using astrophysical mixing-length theory (Böhm-Vitense 1958) or through various diffusive processes (see Heger et al. 2000, for a thorough discussion). Recent multidimensional simulations of stellar convection (see Arnett et al. 2009, and references therein), however, show a large discrepancy when compared to parameterized one-dimensional models in the case of stellar evolution codes. Indeed there has recently been an effort put forth in the astrophysical community, the so-called Convection Algorithms Based on Simulations or CABS, to derive from multidimensional simulations

a more physically motivated prescription for handling convection in one dimension (Arnett et al. 2008). To date, such methods have not propagated into the XRB-simulation community and a proper treatment of convection, without assumptions, requires multiple dimensions.

Multidimensional simulations of any aspect of XRBs, however, have hitherto been rather restrictive. A burning front can propagate either supersonically as a detonation or subsonically as a deflagration. Full hydrodynamic XRB detonation models in the spirit of Fryxell & Woosley (1982) or Zingale et al. (2001) require a thick ($\sim$ 100 m) accreted helium layer. Such deep layers are only produced by very low accretion rates which are inconsistent with the majority of rates inferred from observations of XRBs and therefore most XRBs are likely deflagrations. For fully compressible hydrodynamics solvers, however, deflagration models are computationally much more expensive than detonation models because of the restrictive timestep requirement due to the slow fluid flow. To overcome this restriction one must somehow filter out the acoustic waves in the system and allow the timestep to be dynamically restricted. Such a method is called a low Mach number approximation method where classical examples are the incompressible fluid and the Boussinesq approximation. To this end, Spitkovsky et al. (2002) used a simple, shallow-water, 2-layer, incompressible fluid to model the vertical structure of a deflagration front and showed how rotation coupled with convection may play an important role in regulating the spread of the front over the surface of the neutron star.

More recently, Lin et al. (2006) developed and applied a low Mach number approximation method to the problem of convective burning at the base of an accreted layer in an XRB system. Their simulations show beautiful Bénard convection cells but are perhaps under-resolved (see the discussion in §3). Their method, however, was only first order accurate in space and time and did not allow for the evolution of the hydrostatic base state, a feature which is needed to capture the expansion of the atmosphere in response to heating. Furthermore, their method was not able to model the surface of the accreted layer which is vital to understanding bursts which exhibit photospheric radius expansion (PRE bursts); such bursts are crucial in determining the stellar properties of neutron stars (Steiner et al. 2010, and references therein).

In this study we use `MAESTRO` (Almgren et al. 2006a,b, 2008, hereafter Papers I-III), a low Mach number approximation code specifically designed for astrophysical flows, to model the convection leading up to an outburst of a pure ^{4}He accretor. `MAESTRO` has already proven useful in modeling the convection in a white dwarf leading up to ignition of a Type-Ia supernovae (Zingale et al. 2009, Paper IV). Recently, `MAESTRO` was augmented with adaptive mesh refinement (Nonaka et al. 2010, hereafter Paper V), which allows for higher computational efficiency by only refining the computational grid in areas of dynamical interest. The reader

is referred to Papers I-III for the details on deriving the low Mach number equation set and especially to Paper V for a full description of the algorithm and its implementation.

The main goals of this paper are to explore and describe the challenges of modeling XRBs in multiple dimensions and to better understand the convective phase that precedes the outburst. In §2 we describe in more detail the current `MAESTRO` algorithm as applied to the XRB problem, in particular the introduction of thermal conduction to the equation set, the use of a time-dependent base state and the introduction of a "volume disprecpancy" correction term to ensure the base state pressure remains thermodynamically consistent with our equation of state. §3 contains an overview of how our one-dimensional initial models are generated and the difficulties of obtaining a solution viable for mapping into multiple dimensions. In §4 we present the results of our studies regarding the strict resolution requirements to properly resolve the burning layer (§4.1), the effects of thermal conductivity (§4.2), the expansion of the base state (§4.3), the effects of the volume discrepancy term (§4.4) and finally we give some analysis of the convective features resulting from thermonuclear burning (§4.5). We give a discussion of the limitations of our results and plans for future work in §5.

2. Method

In this paper we expand the low Mach number equation set derived in Papers I–V to include thermal conduction. The necessary assumption for validity of the generalized system is, as before, that the Mach number, M, of the flow be small. Then we can decompose the pressure, $p(\boldsymbol{x}, r, t)$, into a base state pressure, $p_0(r, t)$, and a perturbational, or dynamic, pressure, $\pi(\boldsymbol{x}, r, t)$, such that $|\pi|/p_0 = O(M^2)$. Here, $\boldsymbol{x}$ represents the horizontal coordinate directions and r represents the radial direction. The perturbations of density and temperature need not be small. In order to filter acoustic waves from the solution, we substitute p_0 for p in all but the momentum equation (see Paper I). The base state is assumed to be in hydrostatic equilibrium, i.e., $\nabla p_0 = -\rho_0 g \boldsymbol{e}_r$, where $\rho_0 = \rho_0(r, t)$ is the base state density, $\boldsymbol{e}_r$ is the unit vector in the outward radial direction, and g is the gravity. Differing from previous Papers, the methodology used in this paper will allow the base state variables to explicitly be functions of time allowing for a response to heating. Also for this paper, we shall assume that gravity is constant in space and time; this plane-parallel approxmiation is valid because the thickness of the accreted layer ($\sim$ 10 m) is much less than the radius of the neutron star ($\sim$ 10 km). Whereas the base state pressure and density are introduced to filter acoustic waves from the system and the base state velocity is used to advect the base state, we introduce a base state for the enthalpy to control the numerical error (see Paper

V).

We recall from Paper V the low Mach number equation set, now with thermal conduction,

$$\frac{\partial(\rho X_k)}{\partial t} = -\nabla\cdot(\rho X_k \boldsymbol{U}) + \rho\dot{\omega}_k, \tag{1}$$

$$\frac{\partial \boldsymbol{U}}{\partial t} = -\boldsymbol{U}\cdot\nabla\boldsymbol{U} - \frac{1}{\rho}\nabla\pi - \frac{(\rho-\rho_0)}{\rho}g\boldsymbol{e}_r, \tag{2}$$

$$\frac{\partial(\rho h)}{\partial t} = -\nabla\cdot(\rho h\boldsymbol{U}) + \frac{Dp_0}{Dt} + \rho H_{\rm nuc} + \nabla\cdot(k_{\rm th}\nabla T), \tag{3}$$

where ρ, $\boldsymbol{U}$, h, p, T and $k_{\rm th}$ are the density, velocity, specific enthalpy, pressure, temperature and thermal conductivity. The species are represented by their mass fractions, X_k, along with their associated production rates, $\dot{\omega}_k$, and $H_{\rm nuc}$ is the total specific energy generation rate. The system is closed with a general stellar equation of state (EOS) (Timmes & Swesty 2000) which can be re-posed as an elliptic divergence constraint on the velocity field (see Paper III):

$$\nabla\cdot(\beta_0\boldsymbol{U}) = \beta_0\left(S - \frac{1}{\overline{\Gamma}_1 p_0}\frac{\partial p_0}{\partial t}\right), \tag{4}$$

where β_0 is a density-like variable,

$$\beta_0(r,t) = \rho(0,t)\exp\left(\int_0^r \frac{1}{\overline{\Gamma}_1 p_0}\frac{\partial p_0}{\partial r'}\,dr'\right), \tag{5}$$

and $\overline{\Gamma}_1$ is the lateral average of $\Gamma_1 = (d\log p/d\log\rho)$ at constant entropy. The lateral average of a quantity ϕ is defined as

$$\overline{\phi}(r,t) = \frac{1}{A(\Omega_H)}\int_{\Omega_H}\phi(\boldsymbol{x},r,t)\;dA, \tag{6}$$

where Ω_H is a region at constant height and $A(\Omega_H)\equiv\int_{\Omega_H}dA$ with dA being an area measure. The expansion term, S, in (4) accounts for local compressibility effects resulting from nuclear burning, external heat sources, compositional changes and, now, thermal conduction:

$$S = -\sigma\sum_k \xi_k\dot{\omega}_k + \frac{1}{\rho p_\rho}\sum_k p_{X_k}\dot{\omega}_k + \sigma H_{\rm nuc} + \frac{\sigma}{\rho}\nabla\cdot(k_{\rm th}\nabla T), \tag{7}$$

where $\xi_k \equiv (\partial h/\partial X_k)_{\rho,T,(X_j,j\neq k)}$, $p_\rho \equiv (\partial p/\partial\rho)_{T,X_k}$, $p_{X_k} \equiv (\partial p/\partial X_k)_{T,\rho,(X_j,j\neq k)}$ and $\sigma \equiv p_T/(\rho c_p p_\rho)$ with $p_T \equiv (\partial p/\partial T)_{\rho,X_k}$, and $c_p \equiv (\partial h/\partial T)_{p,X_k}$.

In practice, the temperature gradient in the thermal conduction terms in (3) and (7) is determined by applying the chain rule to the EOS, written in the form $h = h(p_0,T,X_k)$:

$$\nabla T = \frac{1}{c_p}\nabla h - \frac{h_p}{c_p}\nabla p_0 - \sum_k \frac{\xi_k}{c_p}\nabla X_k, \tag{8}$$

where $h_p \equiv (\partial h/\partial p)_{T,X_k}$. This is done so that we can form a diffusion equation in enthalpy which can be solved using our multigrid solver. Appendix A.1 describes the algorithmic implementation of our implicit solve for these new terms. We describe a test problem for the diffusion solver, diffusion of a Gaussian pulse in two-dimensions, in Appendix B.

An additional change from the `MAESTRO` algorithm as outlined in Paper V is the inclusion of a "volume discrepancy" term, f. When using the divergence constraint from (4), the system may suffer mild numerical instability which causes the base state pressure, p_0, to drift from the full state pressure obtained from the EOS, $p_{\rm EOS} = p(\rho, h, X_k)$ (Pember et al. 1998). To correct for this drift, (4) is augmented with a term which forces the system back to satisfying the EOS:

$$\nabla \cdot (\beta_0 \boldsymbol{U}) = \beta_0 \left(S - \frac{1}{\overline{\Gamma}_1 p_0} \frac{\partial p_0}{\partial t} - \frac{f}{\overline{\Gamma}_1 p_0} \frac{p_0 - p_{\rm EOS}}{\Delta t} \right), \tag{9}$$

where $0 \leq f \leq 1$. See Appendix A.2 for more details and see §4.4 for the effect this term has on the evolution of the system.

3. Initial Models

We begin our calculations by generating a one-dimensional, plane-parallel initial model of the accreted layer in hydrostatic (HSE) and thermal equilibria on the surface of a neutron star. We assume a ^{4}He layer is accreted on top of a ^{56}Fe neutron star with a trace abundance ($\sim 10^{-10}$) of ^{12}C. We choose a pure ^{4}He accretor both because the corresponding nuclear reaction network, 3α burning, is simple compared to the slow, β-decay-limited burning processes in bursts involving H, and because ultra-compact XRB sources are possible pure ^{4}He accretors (4U 1820-30, for example; Cumming (2003)). We include the forward and reverse 3α reaction rates as given in Caughlan & Fowler (1988) with electron screening contributions from Graboske et al. (1973) for the weak regime and from Alastuey & Jancovici (1978) for the strong regime.

There are several approaches to one-dimensional model generation in the literature. Through our studies we have found that some methods work better than others when used in multidimensional simulations. Below, we describe two approaches to model generation and the issues involved with evolving them in multiple dimensions.

3.1. Semi-Analytic Models

The semi-analytic approach to model generation involves integration of the heat equation and an entropy equation,

$$\frac{dT}{dy} = \frac{3\kappa F}{4acT^3} \tag{10}$$

$$\frac{dF}{dy} = 0, \tag{11}$$

where c is the speed of light, a the radiation constant, κ the opacity (including radiative and conductive contributions), F the outward heat flux and $y(r) = -\int \rho(r')dr'$ the column-depth (see Cumming & Bildsten 2000, for details of this method). Note that for simplicity Equation (11) neglects any compressional heating contributions and assumes the accreted material is not burning during the accretion phase. One can add a constant flux, $F_{\rm const}$, to the accreted layer to approximate energy release from both the deep crustal heating and the neglected compressional heating terms; in our studies we set $F_{\rm const} = 200$ keV per nucleon. The integration starts at the top of the ^{4}He atmosphere (arbitrarily at $y_{\rm top} = 10^3$ g cm^{-2}) where a radiative zero solution is assumed, and continues until the thin shell instability condition (Fushiki & Lamb 1987),

$$\frac{d\epsilon_{3\alpha}}{dT} > \frac{d\epsilon_{\rm cool}}{dT}, \tag{12}$$

is reached at $y = y_{\rm base}$. The local cooling rate is approximated from (10) and (11) as

$$\epsilon_{\rm cool} \approx \frac{acT^4}{3\kappa y^2}. \tag{13}$$

When (12) is attained, the composition for $y > y_{\rm base}$ is switched to ^{56}Fe and integration of (10) and (11) resumes until a thick enough substrate is formed such that $y_{\rm base}$ is sufficiently far from the bottom of the computational domain, $y(r = 0) = 10^{12}$ g cm^{-2} in our studies. Care is also taken to ensure that the temperature gradient is never superadiabatic.

The approximation, (13), works well in one dimension because the only efficient way the system can cool (neglecting weak reactions) is via conduction and radiation which enter through the opacity. When more spatial dimensions are added to the system and there is heating from below from nuclear reactions, the fluid is free to overturn and cool via convection. Now we have a situation where the local multidimensional cooling rate, $\epsilon_{\rm cool,\ multi\text{-}d} = \epsilon_{\rm cool} + \epsilon_{\rm conv}$, exceeds the initial approximation and (12) is no longer be satisfied. Therefore, such a semi-analytic model is no longer close to runaway and to evolve the system in multiple dimensions until (12) is reached is intractable even with the advantages of a low Mach number approxmation code.

3.2. `Kepler`-supplemented Models

One way to overcome the difficulties with evolving the model described in the previous section in multiple dimensions is to explicitly include an *effective* convective cooling term in the approximation to the local cooling, (13). To that end, we make use of the stellar evolution code, `Kepler` (Weaver et al. 1978), which takes as its starting data our previous semi-analytic model for the accreted atmosphere and constructs the remainder of the neutron star with $R_{\rm ns} = 10$ km and $M_{\rm ns} = 1.87 M_\odot$. The system is then allowed to evolve in one dimension and the *effective* convective cooling is provided from mixing-length theory. Nuclear burning heats the base of the layer and the convection prescription develops a well-mixed and adiabatic region of ^{12}C ash overlying the ^{4}He base. This results in a model which is much closer to satisfying the thermal instability criterion, (12), when mapped into multiple dimensions..

The data from `Kepler` is given in a Lagrangian (mass) coordinate system and we need to convert to a Eulerian (physical) coordinate system. We use a procedure similar to that found in Zingale et al. (2002) to ensure our initial model is in HSE. Given the density, temperature and composition from the `Kepler` evolution, we call our EOS to get the pressure. We then discretize the HSE equation and solve for the non-uniform Eulerian grid spacing corresponding to the Lagrangian grid points,

$$r_i = r_{i-1} - \frac{1}{g} \frac{p_i - p_{i-1}}{\frac{1}{2}\left(\rho_i + \rho_{i-1}\right)}, \tag{14}$$

where we set $r_1 = 0$ to complete the description of the grid. The transition from the pure ^{56}Fe neutron star (at $r_{\rm trans}$) to the ^{4}He atmosphere (at $r_{\rm trans+1}$) is a step function as a result of the initial Lagrangian data. To smooth the interface, we add n uniformly distributed coordinate points between $r_{\rm trans}$ and $r_{\rm trans+1}$. The temperature at these new points is linearly interpolated between $T_{\rm trans}$ and $T_{\rm trans+1}$. Then $X(^4{\rm He})$ and $X(^{12}{\rm C})$ at the new points are filled with a tanh profile:

$$\phi_i = \alpha \tanh\left(\frac{r_i - r_{\rm c}}{\varphi}\right) + \phi_{\rm c} \tag{15}$$

where $\alpha = \left(\phi_{\rm trans+1} - \phi_{\rm trans}\right)/2$, $r_{\rm c} = \left(r_{\rm trans} + r_{\rm trans+1}\right)/2$, $\phi_{\rm c} = \left(\phi_{\rm trans} + \phi_{\rm trans+1}\right)/2$ and φ is a parameter to set the smoothness. $X(^{56}{\rm Fe})$ is then found from the constraint $\sum_k X_k = 1$, and p and ρ are found by iterating with the EOS and (14) at these new points. This smoothed model is then linearly interpolated onto a completely uniform grid, with $r_i = r_{i-1} + \Delta r$, and is again iterated into HSE using (14) and our EOS. Values of $n = 50$ and $\varphi = 3$ were used to smooth the models presented in this work.

Figure 1 shows the result of this procedure for two models which were evolved in `Kepler` until the base of the ^{4}He atmosphere had reached a temperature of 3.67×10^8 K (solid line, hereafter referred to as the `cold` model) and 5.39×10^8 K (dotted line, hereafter referred

to as the `hot` model). The `cold` model has a peak in ^{12}C production around $r = 382$ cm (i.e. the base of the ^{4}He layer in both models) which appears smoothed out in the more evolved `hot` model. Both models, however, have an extended region of well mixed ^{12}C which extends to $r = 624$ cm ($r = 812$ cm) for the `cold` (`hot`) model. These initial models contain no velocity information from the `Kepler` simulations. We therefore make no assumptions about the nature of the convection when the models are mapped into multiple dimensions in `MAESTRO`.

3.3. Sponging and the Anelastic Cutoff Density

As explained in Paper III, the sharp drop-off in density at the surface of the star may create a large velocity field in the dynamically unimportant region above the surface which would reduce the efficiency of our low Mach number algorithm. We therefore apply a sponging technique which dampens such spurious velocity fields. The velocity in the sponged region is given as $\boldsymbol{U}^{\rm new} = \boldsymbol{U}^{\rm old} * \texttt{sponge}$ where the sponge "turns on" over the interval $r_{sp} = r(\rho = \rho_{sp})$ to $r_{tp} = r(\rho = \rho_{tp})$:

$$\texttt{sponge} = \begin{cases} 1, & r \le r_{sp}, \\ \frac{1}{2}\left(1 - \texttt{sponge}_{min}\right)\cos\left[\pi\frac{r-r_{sp}}{r_{tp}-r_{sp}}\right] + \frac{1}{2}\left(1 + \texttt{sponge}_{min}\right), & r_{sp} < r \le r_{tp}, \\ \texttt{sponge}_{min}, & r_{tp} < r, \end{cases} \quad (16)$$

where the free parameters $\texttt{sponge}_{min} = 0.1$ and $\rho_{sp} = 25\rho_{tp}$ for the current paper[1]. Figure 2 shows the profile of the sponge for the `cold` model.

Also outlined in Paper III is the description of an "anelastic cutoff" density, $\rho_{\rm anelastic}$, below which we determine β_0 by keeping the ratio β_0/ρ_0 constant so as to minimize any spurious wave generation at the edge of the star. There is another cutoff, the "low density cutoff" $\rho_{l.d.c}$, below which the base state is held constant. For this paper, we set $\rho_{tp} = \rho_{\rm anelastic} = \rho_{l.d.c} = 10^4$ g / cm^3. The vertical grey lines correspond to the location of r_{sp} and the vertical black lines correspond to the location of r_{tp} for each of the initial models in Figure 1. Note that as the system evolves it is free to expand thus changing the location and extent of the sponge turn-on region and consequently the locations of the density cutoffs.

[1]Note that the form of this sponge is similar to that presented in §4.3.1 of Paper III but with $\kappa\Delta t = 1$ at each timestep.

4. Results

We describe below the results of mapping the Kepler-supplemented models into MAESTRO in two dimensions, $(x,\ r)$, and the system's subsequent evolution. The one-dimensional model is simply copied laterally across the domain such that $\phi(x, r) = \phi_{\text{one-d}}(r)$ for all variables ϕ which describe the system. In what follows, unless otherwise stated, the subscript "max" refers to the maximum value of a quantity in the computational domain at a given timestep. Analogous to (6), we define the lateral average as a function of radius, $\langle\phi\rangle_r$, of a quantity ϕ in two dimensions by

$$\langle\phi\rangle_{r_j} = \frac{1}{N_j}\sum_{i=1}^{N_j}\phi_{i,j} \tag{17}$$

where $\phi_{i,j} = \phi(x_i, r_j)$ and N_j is the total number of grid zones in the lateral, x, direction at height r_j. The root mean square deviation from the mean, $(\delta\phi)_r$, is then

$$(\delta\phi)_{r_j} = \left(\frac{1}{N_j}\sum_{i=1}^{N_j}\left(\langle\phi\rangle_{r_j} - \phi_{i,j}\right)^2\right)^{1/2}. \tag{18}$$

For all of our calculations, opacities are calculated using Frank Timmes' publicly available conductivity routine which includes contributions from radiation and electron conduction processes as explained in Timmes (2000).[2] The boundary conditions for all simulations are periodic in the lateral, x, directions, outflow at the upper r boundary and slip-wall at the lower r boundary. An advective CFL number of 0.7 was used in all of our simulations.

As previously mentioned, we do not obtain any velocity information about the convective zone from the Kepler models; our system is initially static. For convection to begin, the symmetry of the system must, therefore, be broken. This can be accomplished either by placing a small perturbation at the base of the ^{4}He layer or by allowing numerical noise to seed the convective cells. Neither approach is advantageous over the other, both giving quantitatively similar steady-state convective flow fields; we utilize both approaches in our studies and when perturbing we place a small ($\Delta T/T = 10^{-5}$) Gaussian temperature perturbation laterally centered at height $r = 384$ cm to break the initial symmetry of the problem.

[2]Source code for this routine can be found at http://cococubed.asu.edu/code_pages/kap.shtml.

4.1. Resolution Requirements

To date, the only other paper in the literature regarding multidimensional simulations of XRBs as deflagrations, Lin et al. (2006), used a finest resolution of 5 cm zone^{-1}. They presented multidimensional results at 5, 7.5 and 10 cm zone^{-1} resolutions and remarked that there is a "tendency toward convergence with increasing resolution" based on the time to reach the peak energy generation rate. Comparing $(H_{\rm nuc})_{\rm max}$ for our `cold` model with the "$(\rm EGR)_{\rm max}$" of Lin et al. (2006) (see their Figure 13) at the same resolutions, we should be ~ 0.05 s from reaching the peak of the energy generation rate. Figure 3 shows the evolution of $(H_{\rm nuc})_{\rm max}$ as a function of time for the `cold` model at the resolutions under question with a single level of refinement. In the 7.5 and 10 cm zone^{-1} cases the system initially heats up thus increasing its energy generation rate, but around $t = 7.5$ ms, however, the convection produced from this heating is well established and the system begins to cool and the energy generation weakens. For the 5 cm zone^{-1} resolution model, the system heats for ~ 10 ms before convection competes with the nuclear burning and the energy generation rate levels off. This stabilization period lasts about 15 ms before the system begins to cool, but at a much slower rate than in the more coarsely refined simulations. These $(H_{\rm nuc})_{\rm max}$ trends are drastically different from the results of Lin et al. (2006) which continued to rise in a rather nonlinear but smooth fashion at all three resolutions.

Furthermore, the burning layer at the base of the accreted material is very thin. The top panel of Figure 4 shows the $\langle H_{\rm nuc}\rangle_r$ profile for the `cold` model for the same resolutions as the previous figure at $t = 1$ ms. Even at this early time there is a 25% spread in the peak value of $\langle H_{\rm nuc}\rangle_r$ for these resolutions. The bottom panel shows the same profile but at several higher resolutions. There appears to be a bi-modality in the peak value of $\langle H_{\rm nuc}\rangle_r$: for resolutions of 4 cm zone^{-1} and coarser this value is $\sim 3.25 \times 10^{17}$ erg g^{-1} s^{-1} whereas for the finer resolution simulations it is $\sim 1.5 \times 10^{17}$ erg g^{-1} s^{-1}. In addition, the shape of the profile near peak converges with increasing resolution; the 0.25 and 0.5 cm zone^{-1} resolution simulations look qualitatively similar. We therefore claim that the burning layer is not properly resolved unless a resolution of 0.5 cm zone^{-1} is used; this is the resolution used in the burning layer for all of our further studies in this paper. It is important to note that this resolution requirement is an order of magnitude higher than what has been previously presented in the literature and therefore significantly increases the computational cost of our XRB simulations.

Under-resolving the burning layer artificially boosts the energy generation rate which in turn over-drives convection. Figure 5 shows a close-up of the ^{12}C mass fraction after 10 ms of evolution of the `cold` model at 0.5 (`a`), 2 (`b`), 4 (`c`) and 7.5 cm zone^{-1} (`d`) resolutions. The base of the burning layer is located in the bottom-most green region (just below the

magenta) in panel a. All four simulations give a well-mixed carbon region above the burning layer; the extent of the convective zone increases with resolution with the 7.5 cm zone^{-1} convective zone extending 30% further than the 0.5 cm zone^{-1} simulation's convective zone. The amount of convective overshoot is much more sensitive to resolution. The 0.5 cm zone^{-1} simulation shows very little evidence of overshooting while the 7.5 cm zone^{-1} simulation has an overshoot region which is larger in physical extent than it's corresponding convective region above the burning layer.

4.2. Effects of Thermal Diffusion on the Burning Layer

As explained in §1, the burning front during an XRB likely propagates as a subsonic flame, the speed of which will be regulated by the rate of thermal diffusion across the front. At the resolution required to resolve the thin burning layer (see previous section) it is currently intractable to evolve the system until flame ignition. We can, however, investigate the effects of thermal diffusion on the stable burning which occurs in the burning layer. Figure 6 shows these effects in $(H_{\rm nuc})_{\rm max}$ (solid lines) and the location of this maximum (dashed lines) as a function of time for the hot model at early times both with (green) and without (blue) thermal diffusion. The $(H_{\rm nuc})_{\rm max}$ evolution is similar for both cases with the magnitude in general being larger for the case of no diffusion. Looking at the vertical location where the maximum occurs, we see that this is in general coincident with the peak burning occuring in a slightly deeper layer in the atmosphere for the case without diffusion. Without thermal diffusion, the convection is a bit stronger and there is more undershoot.

Say more here...

4.3. Expansion of Base State due to Heating

Having a dynamical base state allows us to capture the large scale expansion of the atmosphere due to heating from nuclear reactions. This differs from the work by Lin et al. (2006) which had a time-independent base state and did not model the top of the accreted atmosphere due to numerical complications with their algorithm. Figure 7 shows the ratio of the base state density to that of the initial ($t = 0$) base state density profile near the surface of the star, defined as $\rho_0 = \rho_{l.d.c}$, for the cold model. The vertical dashed lines represent the location of the surface for each time-value. After 26.6 ms of evolution, the base state has responded to heating from nuclear reactions approximately 4.5 m below the surface by expanding 3.5 cm.

The extent of the expansion is rather small at these early times. However, as the system

progresses towards outburst the energy generation and therefore the rate of expansion will increase. As the system expands, the burning layer becomes less degenerate which may be important for the nucleosynthesis during the outburst. Furthermore, a proper modeling of this expansion during the peak of a PRE burst model may help pinpoint the location of the photosphere with respect to the stellar radius at touchdown, a quantity which plays an important role in using XRBs to measure the mass and radius of the underlying neutron star (Steiner et al. 2010, for example).

4.4. Effects of the Volume Discrepancy Term

In §2 we explained that numerically the base state pressure may drift from the full state pressure which would invalidate the assumptions used to derive the low Mach number equation set. To correct for this drift, we introduced the volume discrepancy term, f, which acts to force the base state pressure back to that of the full state. Figure 8 shows the volume discrepancy term in action by examining the percent difference between the base state and full state pressures as a function of time for various values of f. The left panel shows the maximum value whereas the right panel shows the average value of this percent difference; both the peak and average values show the same trend for a given value of f. After the initital adjustment of the system, the average drift for the case of no volume discrepancy correction ($f = 0$) increases approximately linearly at $\sim 0.1\%$ per ms of evolution. Including the correction term restricts the temporal- and spatial-averaged value of the drift to $\lesssim 0.02\%$.

For nonzero f, the oscillatory behavior in the drift is due to the fact that the system may slightly over-correct the base state pressure in a given timestep and then recover in the next step. A larger value of f causes a larger forcing of the drift which tends to be more oscillatory. Furthermore, the plot of the maximum drift shows that a larger value of f can cause a transient drift which exceeds that of the case with no volume discrepancy correction. The selection of an appropriate value for f is a problem-specific endeavor; for the simulations presented here which use a volume discrepancy correction, we used a value of $f = 0.3$.

Should we mention the `use_tfromp` method of decoupling enthalpy entirely? In cases where we use $f = 0$, we set `use_tfromp = T`.

4.5. Convective Dynamics

The adiabatic excess, $\Delta\nabla$, — where

$$\Delta\nabla = \frac{d\ln T}{d\ln P} - \left(\frac{d\ln T}{d\ln P}\right)_s \tag{19}$$

and the subscript s means along an adiabat — is used to measure the extent and evolution of the convective zone. A fluid element is unstable to thermally driven convection when $\Delta\nabla > 0$; it is stable for $\Delta\nabla < 0$.

Figure 9 shows the early evolution of $\Delta\nabla$ for the `cold` model. Each plot covers the spatial range ($0 \leq x \leq 256, 350 \leq r \leq 700$) to focus on the convective region. The initial adjustment of the system (top center panel; $t = 0.4$ ms) causes a mixing of stable (blue) and unstable (red) fluid elements. This mixing produces a region which is marginally convective ($\Delta\nabla \sim 0$; white) with localized pockets of stable and unstable fluid elements as seen in the top right ($t = 0.8$ ms) plot. At later times, these pockets further localize into "dancing donuts" — roughly circular regions with one hemisphere that is stable and the other which is unstable — which are advected with the flow before dispersing into the ambient medium on subconvective timescales, $\sim 10^{-4}$ s. The dancing donuts always have an unstable (red) bottom and a stable (blue) top unless two donuts are merging and interacting in which case the stability distribution becomes skewed.

Figure 10 shows $\Delta\nabla$ for the same simluation as in Figure 9 but at later times. The top panel shows times $t = 18.5, 20.5$, and 23 ms whereas the bottom panel shows times $t = 25, 26$, and 28 ms from left to right. The boxes in these plots outline a single long-lived dancing donut which forms around $t = 18.5$ ms and lasts throughout the remainder of the simulation. Formation of the donut is coorrelated with the formation of stronger filamentary structures which are most clear in the bottom panel plots. These filaments appear to wrap around the solitary donut and restrict the main formation of smaller donuts to the lower boundary of the convective region.

By looking at $\langle\Delta\nabla\rangle_r$ and its spatial derivative, $d\langle\Delta\nabla\rangle_r/dr$, we can get a rough measure of the extent of the convective region. The left panel of Figure 11 shows an example of the typical $\langle\Delta\nabla\rangle_r$ profile in the convective region for the `cold` model. Such profiles are characterized by an almost step-like transition from stable to unstable values of $\Delta\nabla$ followed by an extended region — the convective region — of an approximately flat value of $\Delta\nabla \sim 0$ and then followed another step-like transition from unstable to stable values. We define the extent of the convective region to be where $\langle\Delta\nabla\rangle_r < -0.1$ and $d\langle\Delta\nabla\rangle_r/dr$ has the appropriate sign for each edge (i.e. positive (negative) for the lower (upper) boundary); this prescription allows us to rule out any false positives which might result from a particularly strong donut occuring near the interior of the convective zone. The right panel of Figure 11 shows in grey the extent of the convective zone as a function of time. The horizontal dashed lines represent the initial location of both the lower ($r = 383.75$) and upper ($r = 635.25$) edges of the convective zone. The overall expansion of the uppper boundary is 32.5 cm in ~ 30 ms of evolution; the lower boundary expands downward by 9.5 cm in the same time.

For comparison, Figures 12 and 13 show the ^{12}C mass fraction overplot with velocity vectors for the same simulation and at the same times as in Figures 9 and 10, respectively. Note that each of the dancing donuts in Figures 9 and 10 is associated with a circulation pattern in the velocity field. The initial adjustment of the system causes mixing which smooths the slight over abundance of ^{12}C at the base of the accreted layer present in the initial model (see Figure 1). At late times, the convective region is very well mixed and the ^{12}C mass fraction is nearly laterally homogenous. Furthermore, the circulation pattern associated with the long-lived donut outlined in Figure 10 has grown to a large fraction of the convective zone and is self-interacting because of the periodic boundary conditions. The circulation is counter-clockwise for the large, long-lived donut; this causes a region with positive x-velocity at the below and a region of negative x-velocity above the donut. The positive x-velocity region extends all the way to the lower convective boundary where it causes shearing of the ^{4}He/^{12}C-rich region with the underlying ^{56}Fe region. Consequently, Figure 14 shows that some of the underlying ^{56}Fe neutron star material is churned up into the convective region where it is mixed with the rest of the convective material. The left panel shows the average ^{56}Fe mass fraction profiles starting with the initial model abundance (thick solid line) through $t = 30$ ms (thick dashed line); the intermediate thin solid lines show profiles at the times used in Figures 9 and 10. By $t = 5$ ms, the ^{56}Fe is fairly well-mixed in the convective region. The right panel shows the total mass of ^{56}Fe in the region defined by the initial convective zone. The greatest growth in the total mass occurs, as expected, in the initial adjustment ($t \lesssim 0.6$ ms) and then flattens until large enough structures form such that there is sufficient shearing occuring at the base of the convective boundary. There is only a slight increase in the growth rate for the ^{56}Fe mass around $t = 18.5$ ms where the long-lived donut first appears. This is due to the fact that as the system evolves it goes from many small donuts to a few larger donuts. It is only when the circulation pattern of a particular donut is large enough to strongly interact with the lower convection boundary that we get the shearing and enrichment of the convective region; this occurs around $t \sim 5$ ms. The addition of ^{56}Fe to the convective region has a small but noticable effect on the conductivity of the convective region. This could play an important role in adjusting the flame speed one ignited.

5. Conclusions

We have described some of the challenges and important concepts to keep in mind when performing multidimensional simulations of XRBs. The major results of this project can be summarized as follows:

Is such a blatant listing of the results cromulent? Also, need to say something about thermal diffusion - awaiting more data.

- The local cooling rate estimate, (13), for semi-analytic one-dimensional models should be augmented to include cooling due to convection to get a system which is much closer to thermal instability.
- Properly resolving the burning layer using our initial models requires a spatial resolution of 0.5 cm zone^{-1} which is an order of magnitude higher than what has been presented in the literature for multidimensional models.
- Under-resolving the burning layer leads to dramatic convective overshoot and the burning tends to die out.
- Thermal diffusion
- The `MAESTRO` algorithm we use allows us to capture the expansion of the atmosphere due to heating which will be important in the modeling of PRE burst sources.
- The average thermal gradient in the convective region is nearly adiabatic but there are localized pockets and filamentary structures which are either super- or sub-adiabatic.
- The strong convection interacts with and churns up the underlying neutron star material which slightly alters the conductivity of the convective region.

The width of the computational domain used in our simulations is perfectly adequate for the early evolution of the system; the size of any individual convective cell is initially small with respect to the width of the domain. As the system evolves and the convection becomes more established, the cells grow in size. In our simulations the cells grow to become a significant fraction of the domain width and the flow becomes dominated by a single vortex which interacts with itself through the periodic boundary conditions. Ideally the computational domain should be several pressure scale-heights wide so that we should form multiples of these convective cells which dominate the flow. Given our strict resolution requirements, such a setup was computationally restricted.

We plan to investigate some of these topics in future work while studying mixed H/He bursts. In such bursts the majority of the energy release comes from burning hydrogen; the nuclear reaction rates involved in such burning are less temperature sensitive than the 3-α rate used in the current paper. This may allow for a relaxed resolution requirement for properly resolving the burning layer because the energy generation rate profile should not be as sharply peaked as we have seen in our studies. This would allow for longer time evolution which may allow us to say something about whether or not the convective zone extends all the way to the photosphere near outburst. We will also be able to simulate larger domains where we could address the effects of domain size on the long-term evolution of

the convective region and its ^{56}Fe enrichment. Furthermore, we may begin investigating the effects of unprecedented three-dimensional simulations of the convection that proceeds the outburst in an XRB and compare its properties to our two-dimensional studies.

Acknowledgements Frank for rxn network/conductivities/eos; Ed Brown for the H-burning resolution suggestion; Andrew and Stan for models if they don't want to be co-authors; This work used NYBlue - get their ack. lingo; This work used NERSC's Franklin and Hopper machines - get their ack. lingo; This work was supported by

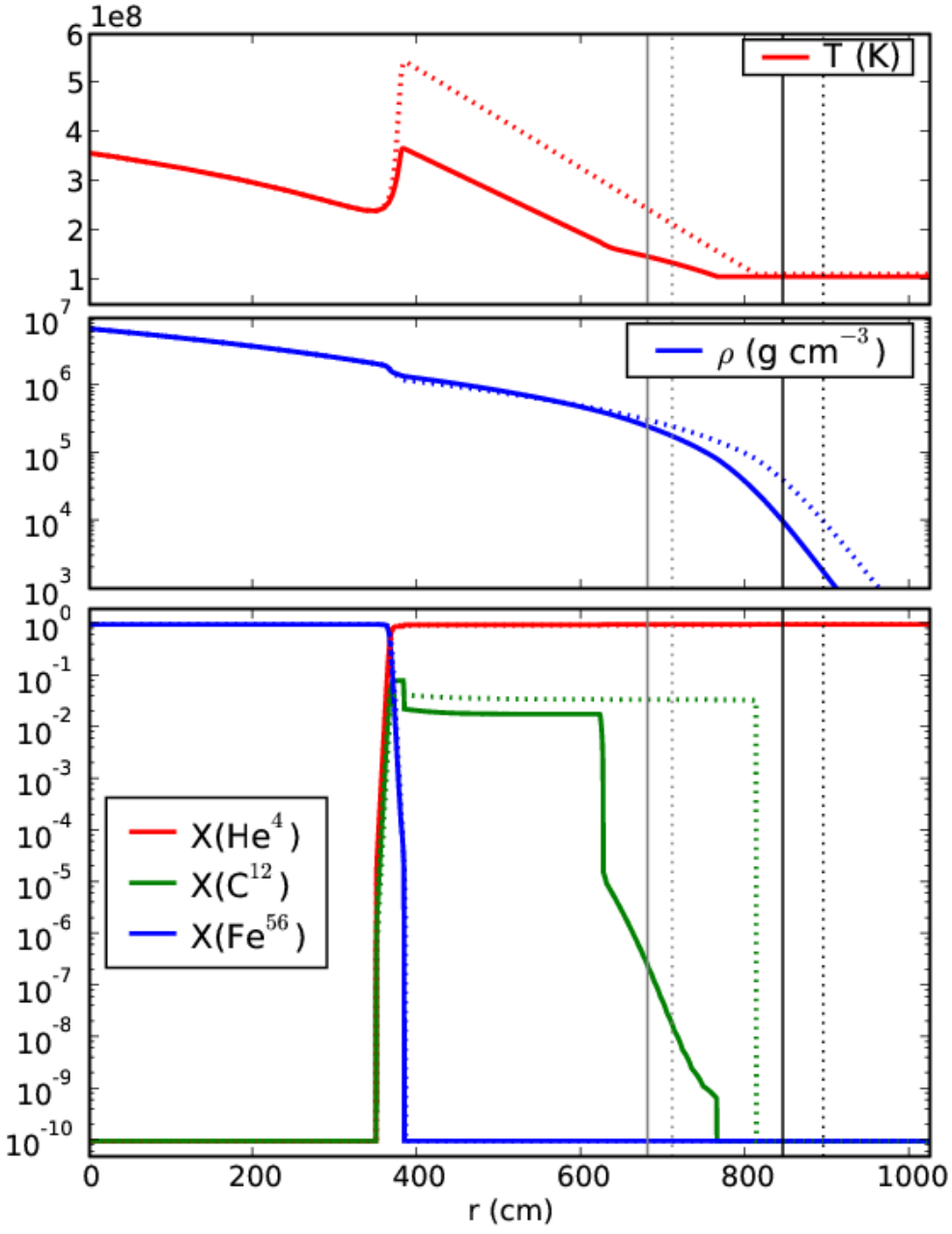

Fig. 1.— `Kepler`-supplemented models as described in the text. Energy release from nuclear burning at the base of the ^{4}He layer has caused the temperature to rise. The `cold` model with solid lines is evolved to a peak $T_{\rm base} = 3.67 \times 10^8$ K and the `hot` model with dotted lines is evolved to a peak $T_{\rm base} = 5.39 \times 10^8$ K. The black vertical lines indicate the location of the anelastic cutoff while the grey vertical lines indicate the location of the beginning of our sponge forcing term for each of the models (see §3.3).

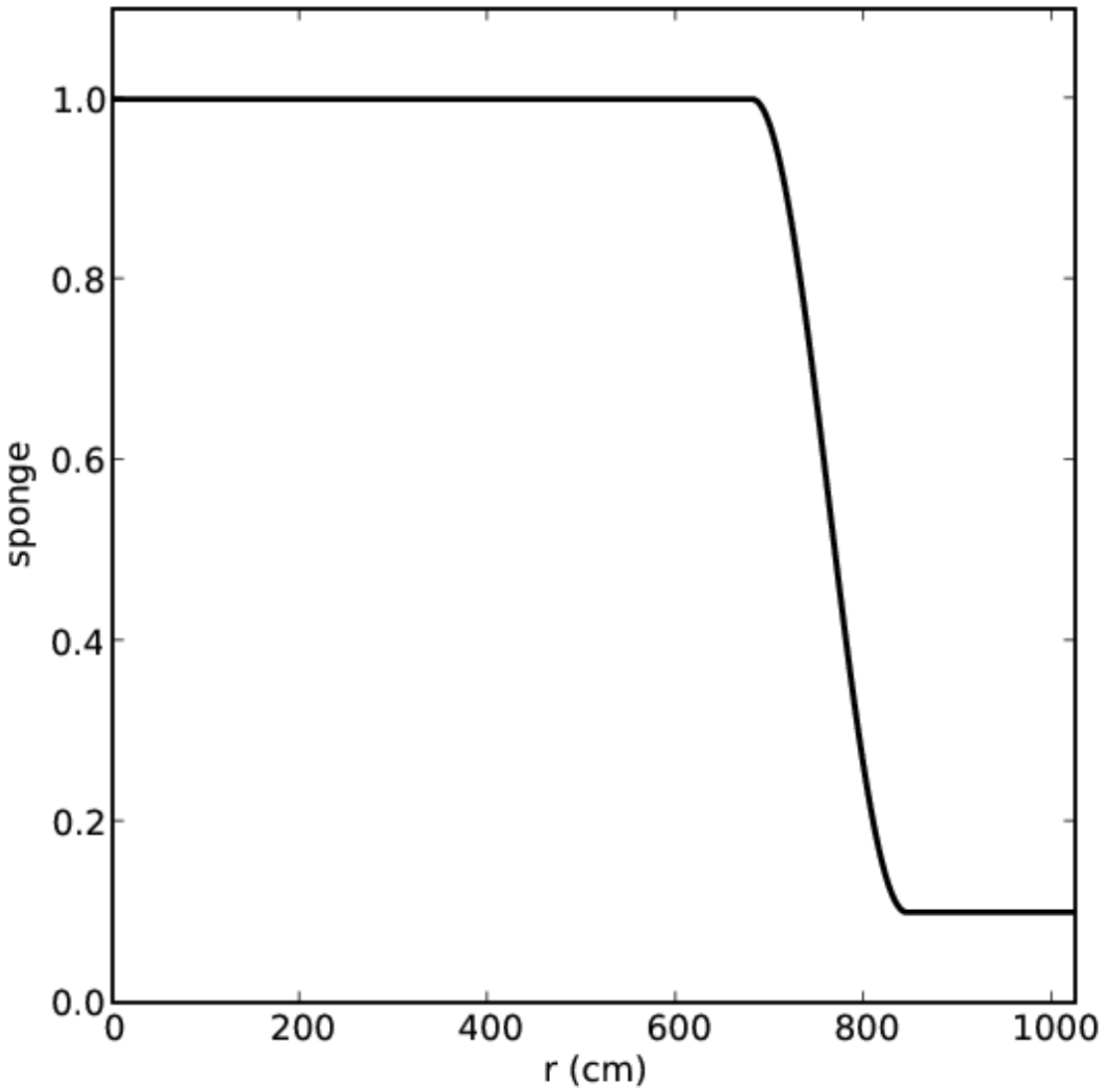

Fig. 2.— Sponge profile for the `cold` model where $r_{sp} = 680$ cm and $r_{tp} = 844$ cm.

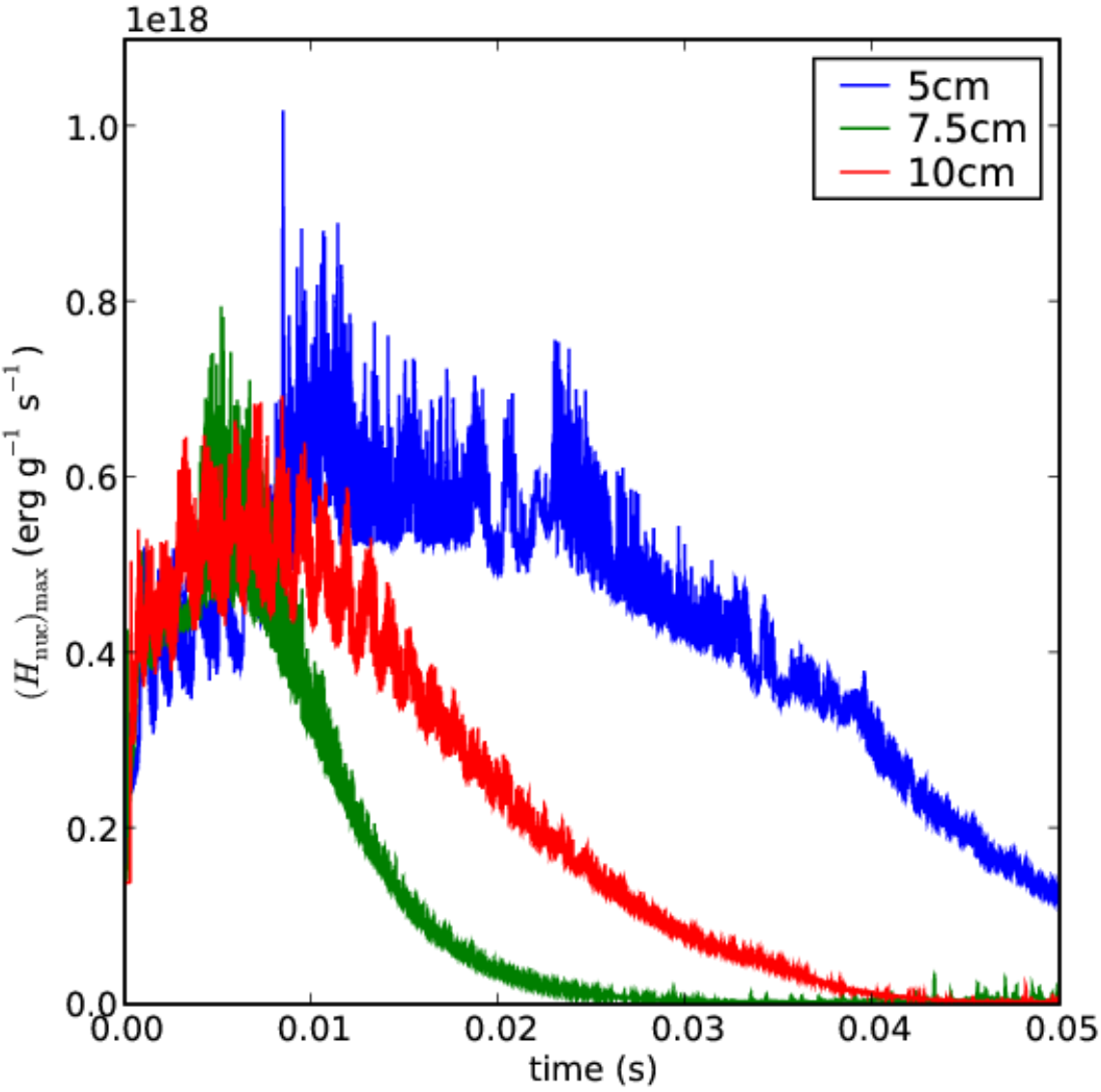

Fig. 3.— Evolution of $(H_{\rm nuc})_{\rm max}$ for the `cold` model at three coarse resolutions. In all cases, the system is initially heating up and we see a rise in the energy generation rate. For the 7.5 and 10 cm zone^{-1} resolution simulations, around $t = 7.5$ ms convective cooling becomes more efficient than the thermonuclear heating and the burning layer tends to die out. The 5 cm zone $^{-1}$ resolution simulation also initially heats but shows a 15 ms period of stable burning before cooling.

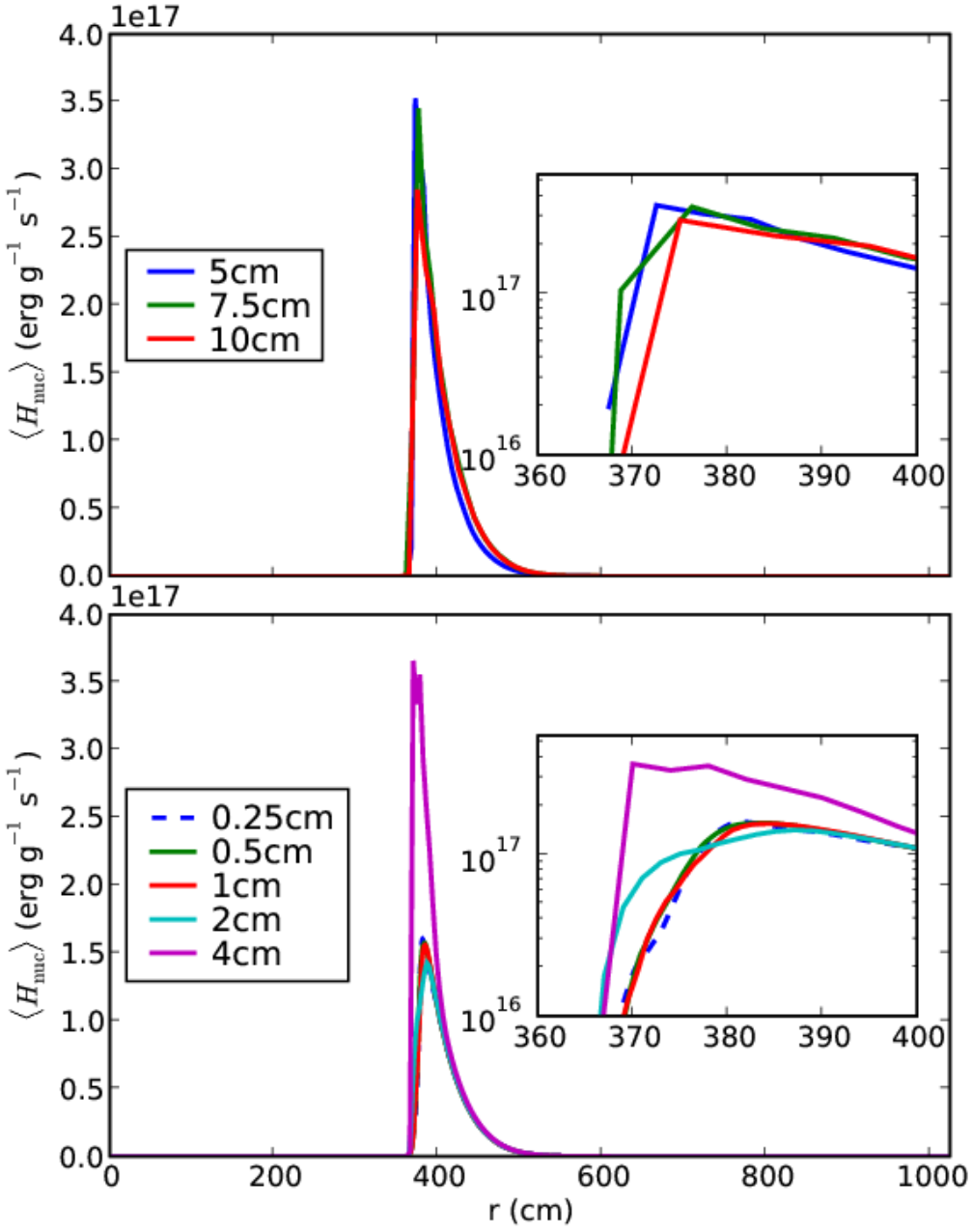

Fig. 4.— Lateral average of $H_{\rm nuc}$ as a function of height for the `cold` model at various resolution models at $t = 1$ ms. Note that the vertical axes of the inset plots are in a logarithmic scale. For clarity, the top panel shows the same resolutions used in Figure 3 and the bottom panel shows more resolved simulations. The peak of the profile at 0.5 cm resolution is qualitatively similar to the peak of the profile at 0.25 cm resolution.

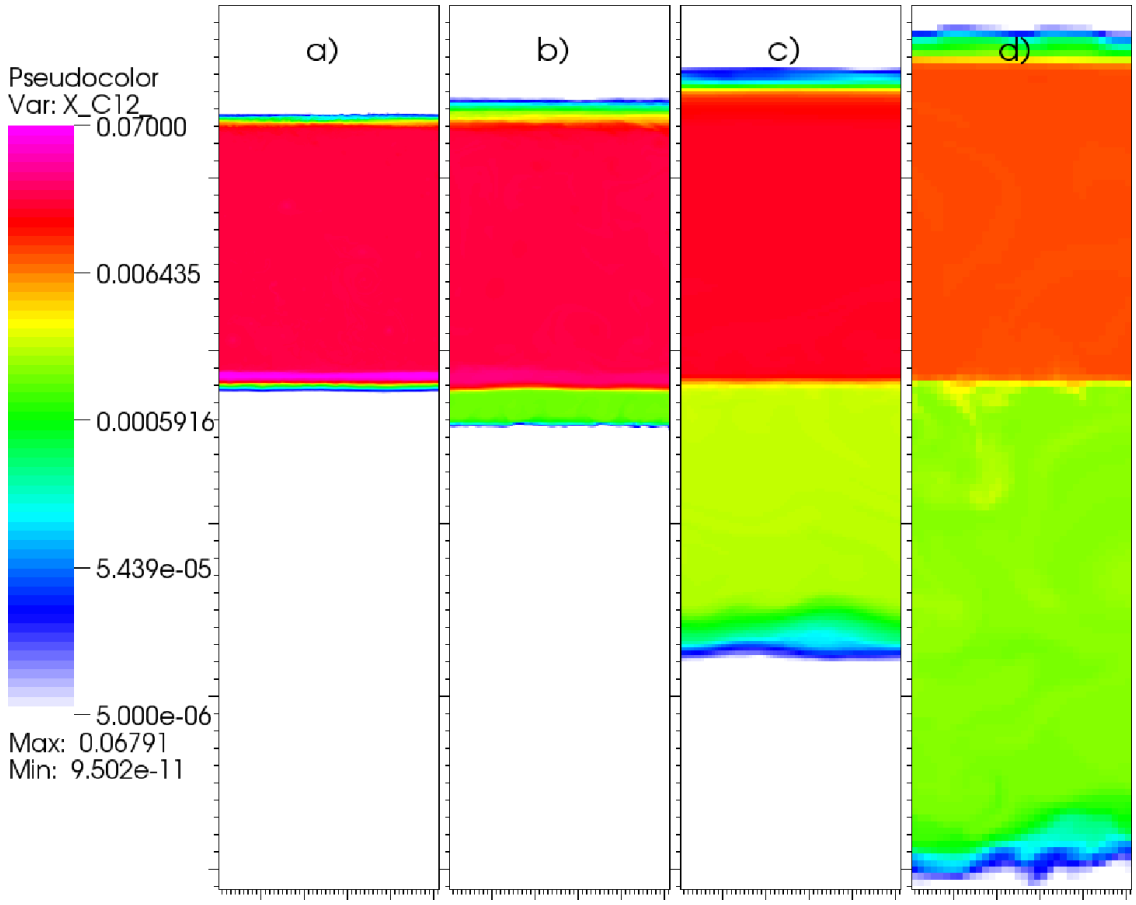

Fig. 5.— Effects of under-resolving convection for the `cold` model. Plotted is the ^{12}C mass fraction after 10 ms of evolution for various resolutions: `a`) 0.5, `b`) 2, `c`) 4 and `d`) 7.5 cm zone^{-1}. Each plot has dimensions 256 cm $\times$ 1024 cm. The grid for panels `b` and `d` were cropped laterally so as to have the same aspect ratio as panels `a` and `c`. The coarse resolution simulations show an extended convective zone and a significant amount of convective overshoot.

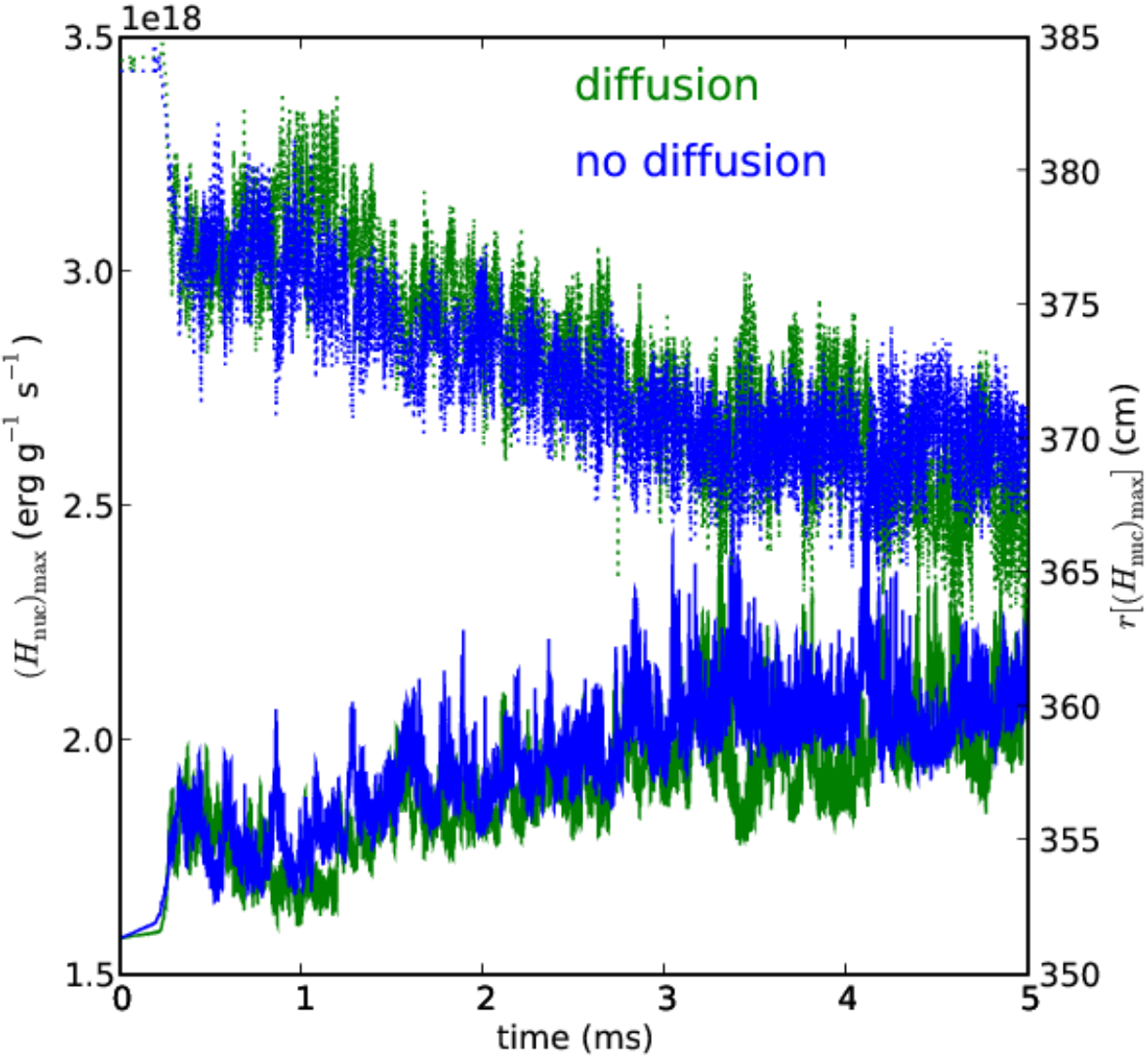

Fig. 6.— Evolution of $(H_{\rm nuc})_{\rm max}$ (solid lines) and its vertical location (dashed lines) as a function of time for the `hot` model both with (green) and without (blue) thermal diffusion.

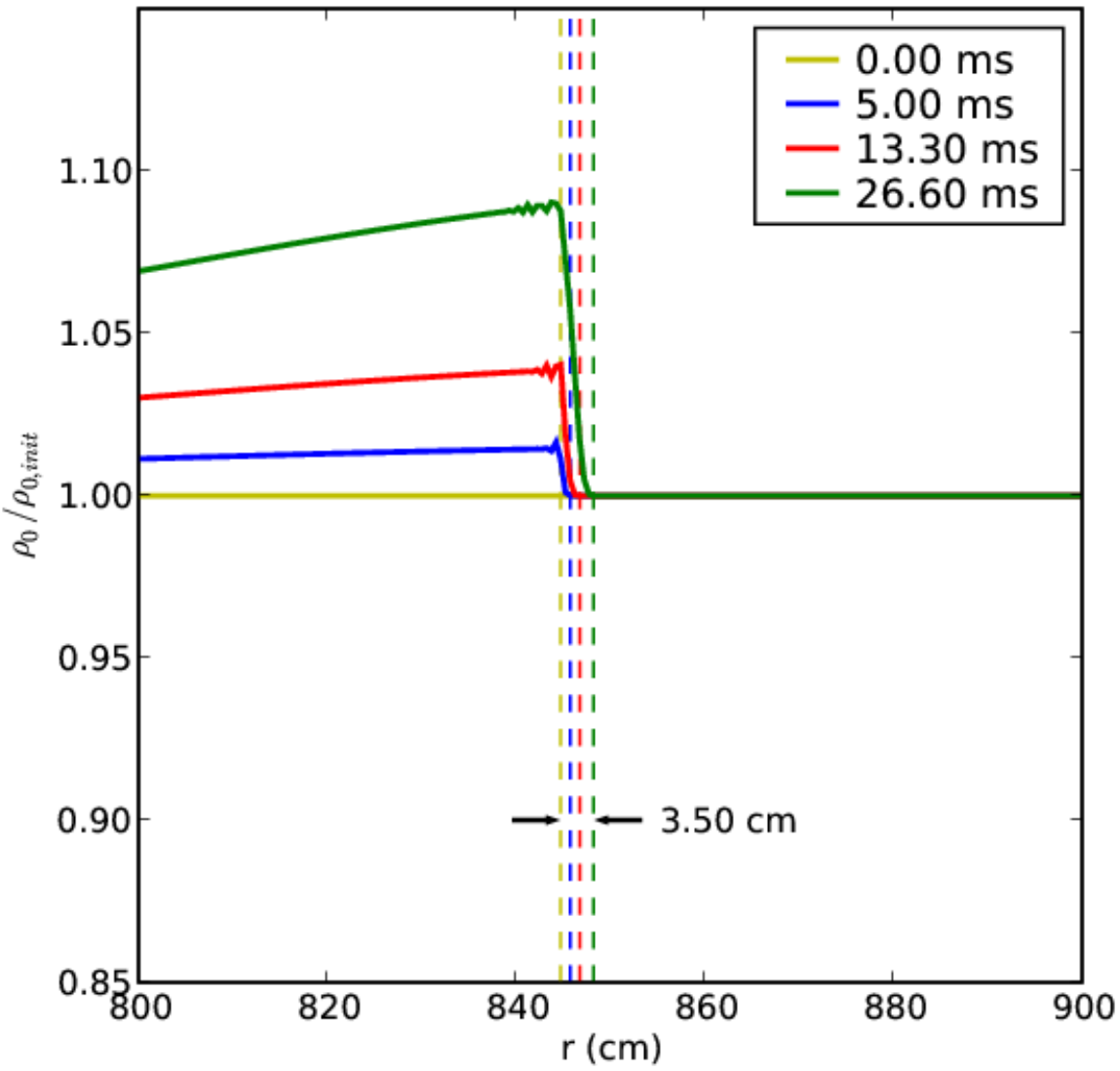

Fig. 7.— Expansion of the base state due to heating. Plotted is the ratio of base state density to the initial ($t = 0$) base state density near the surface of the atmosphere for the `cold` model. We define the surface to be where $\rho = \rho_{l.d.c}$ and it is represented by the vertical lines. The base state has expanded 3.5 cm in 26.6 ms of evolution.

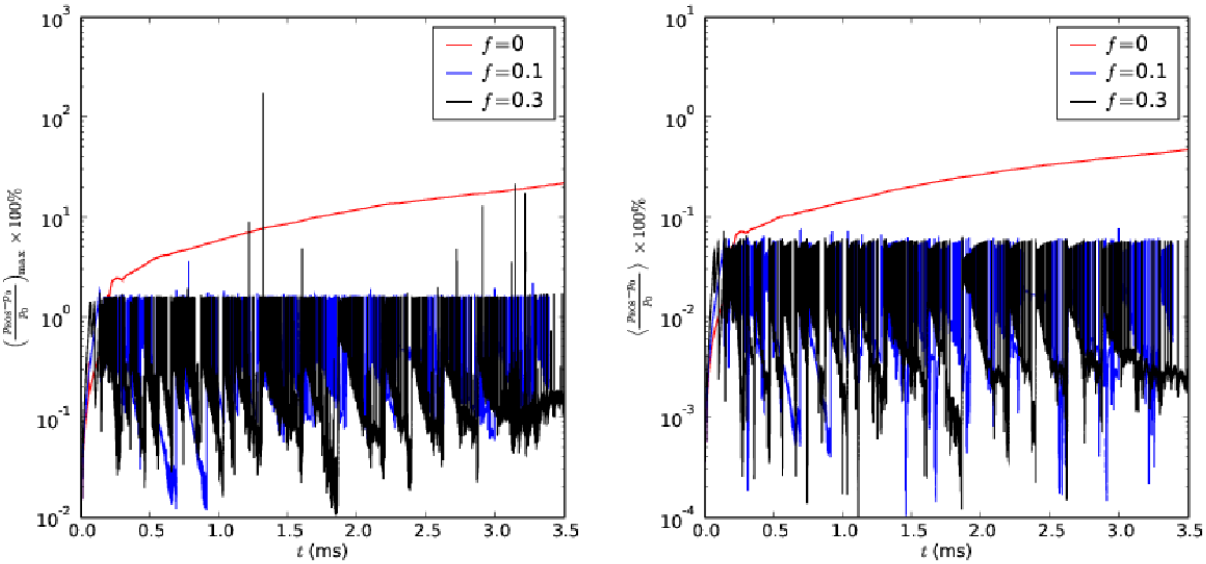

Fig. 8.— Effects of volume discrepancy factor as characterized by the percent difference between the pressure as given by our EOS, $p_{\rm EOS}$, and the base state pressure, p_0, for the `hot` model. The left panel shows the peak value whereas the right panel shows the averaged value of this percent difference.

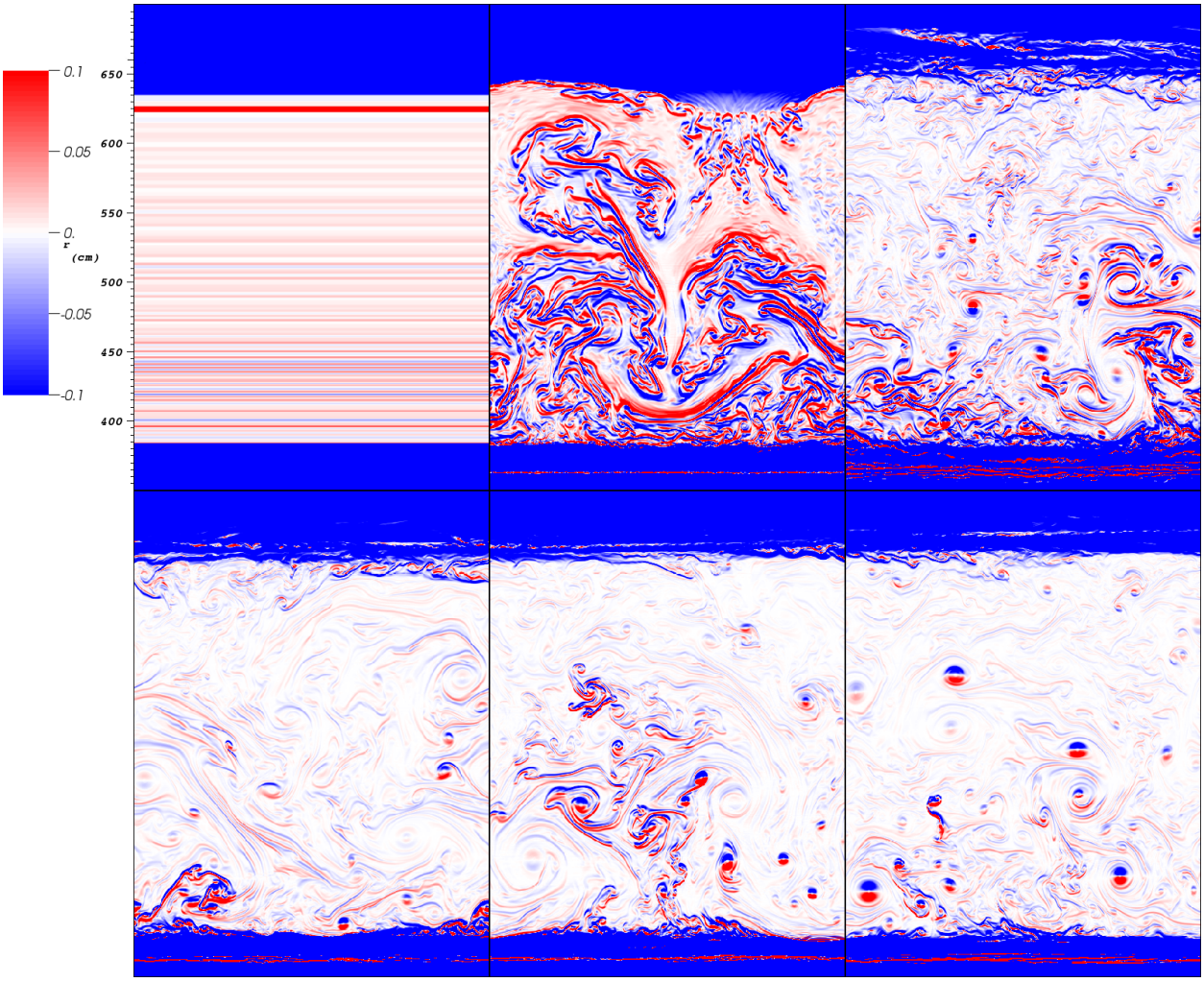

Fig. 9.— Colormap plot of the evolution of the adiabatic excess, $\Delta\nabla$, in the convective region for the `cold` model. The top plots show the system at $t = 0, 0.4$, and 0.8 ms and the bottom plots show $t = 5, 7.5$, and 10 ms from left to right.

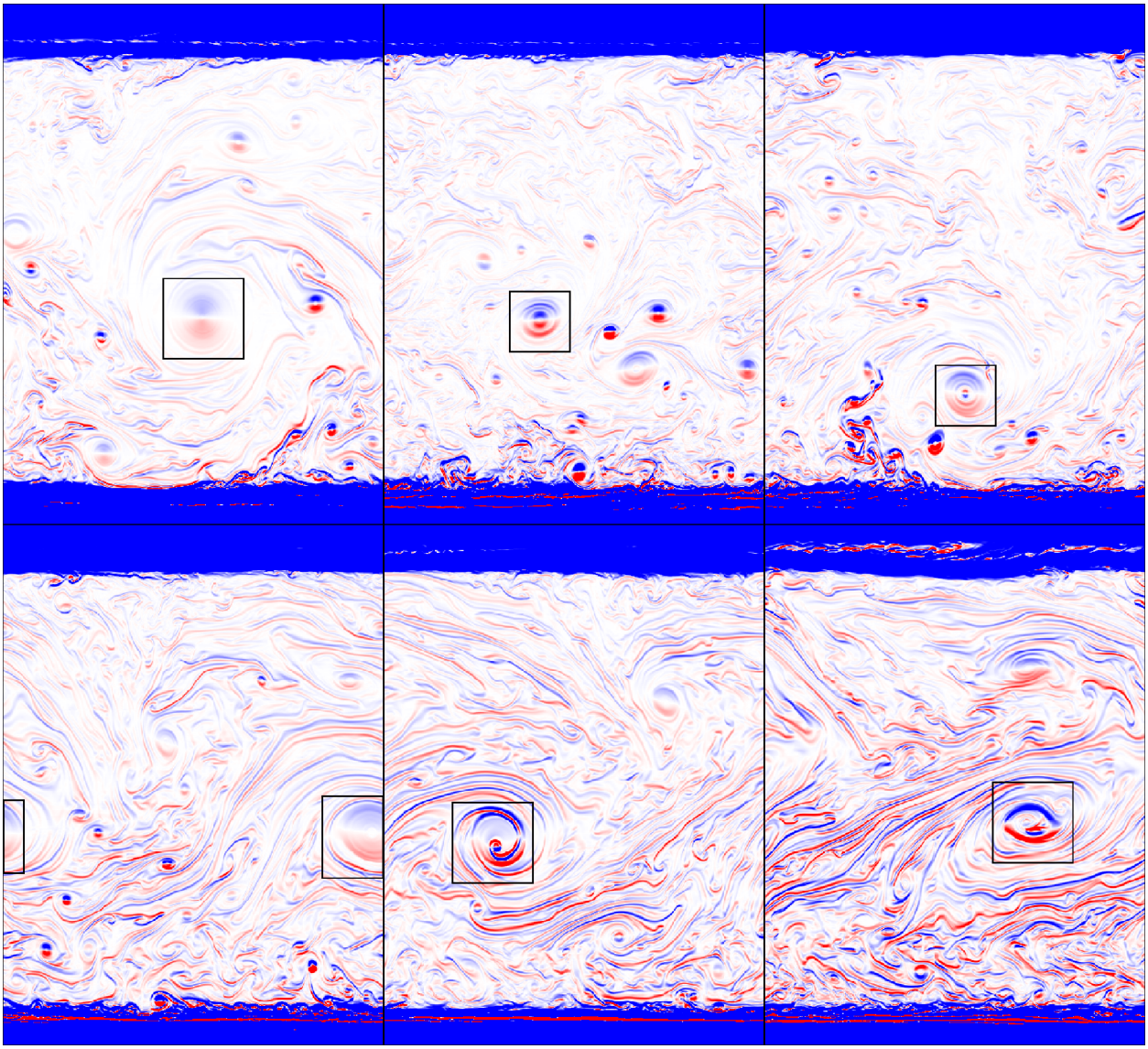

Fig. 10.— Same as Figure 9 but at later times. The top plots show the system at $t = 18.5, 20.5$, and 23 ms and the bottom plots show $t = 25, 26$, and 28 ms from left to right. The boxes show the location of a single feature which lasts for many convective turn-over times.

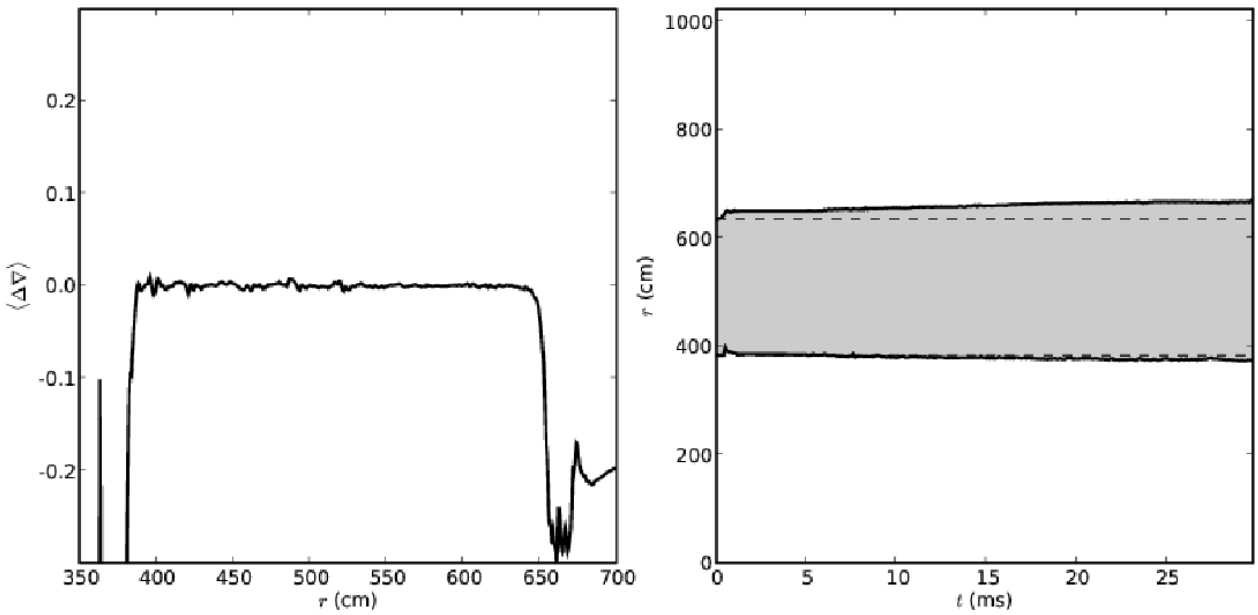

Fig. 11.— Analysis of the extent of the convective region. The left panel shows a typical $\langle \Delta \nabla \rangle_r$ profile for the `cold` model; the extent of the convective zone is based off of the location where the flat region ($\langle \Delta \nabla \rangle_r \sim 0$) goes negative. The right panel shows the extent of the convective region as a function of time. The horizontal dahsed lines mark the locations of the initial convective boundaries.

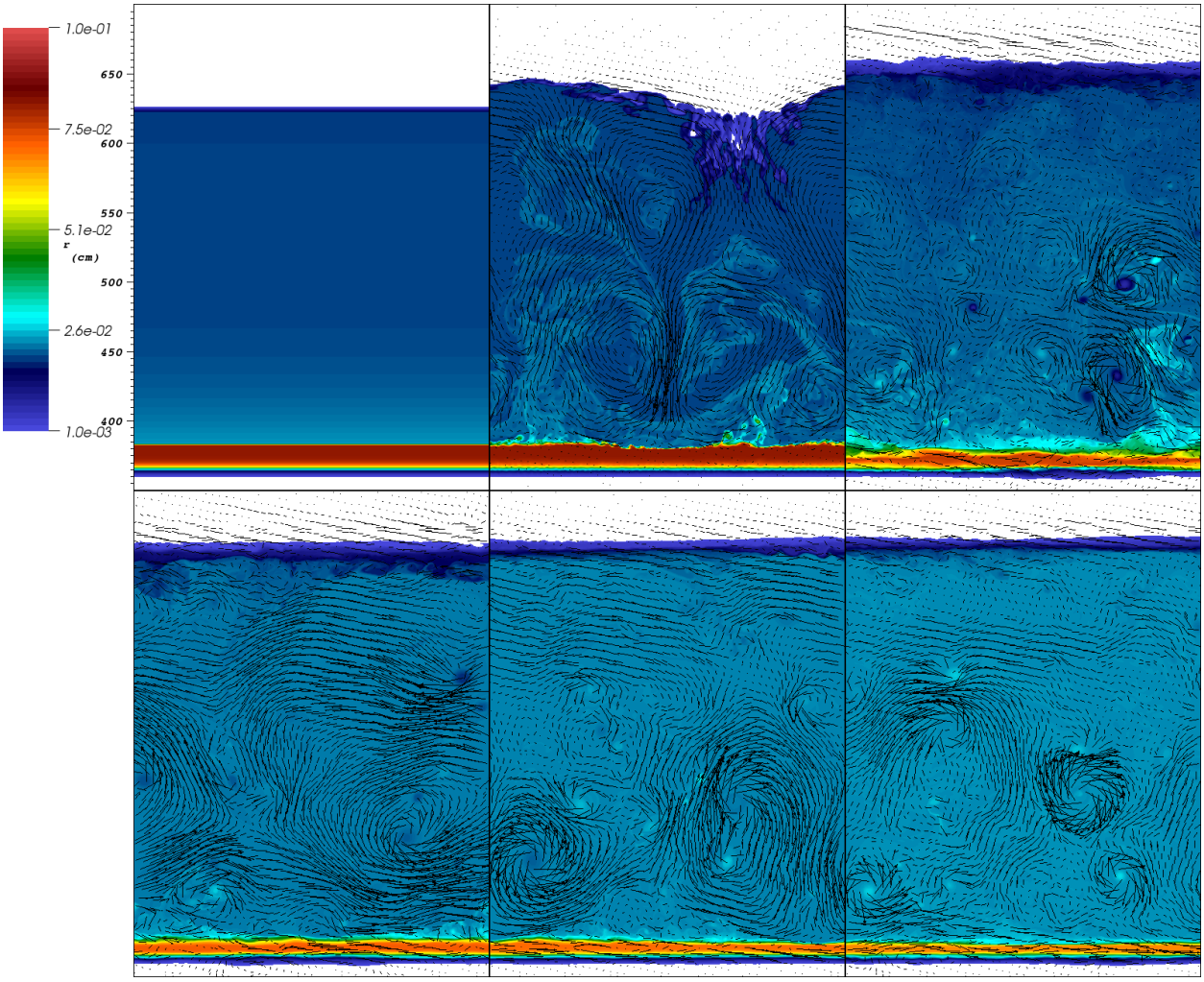

Fig. 12.— Colormap plot of ^{12}C mass fraction overplot with velocity vectors for the same region and times as shown in Figure 9.

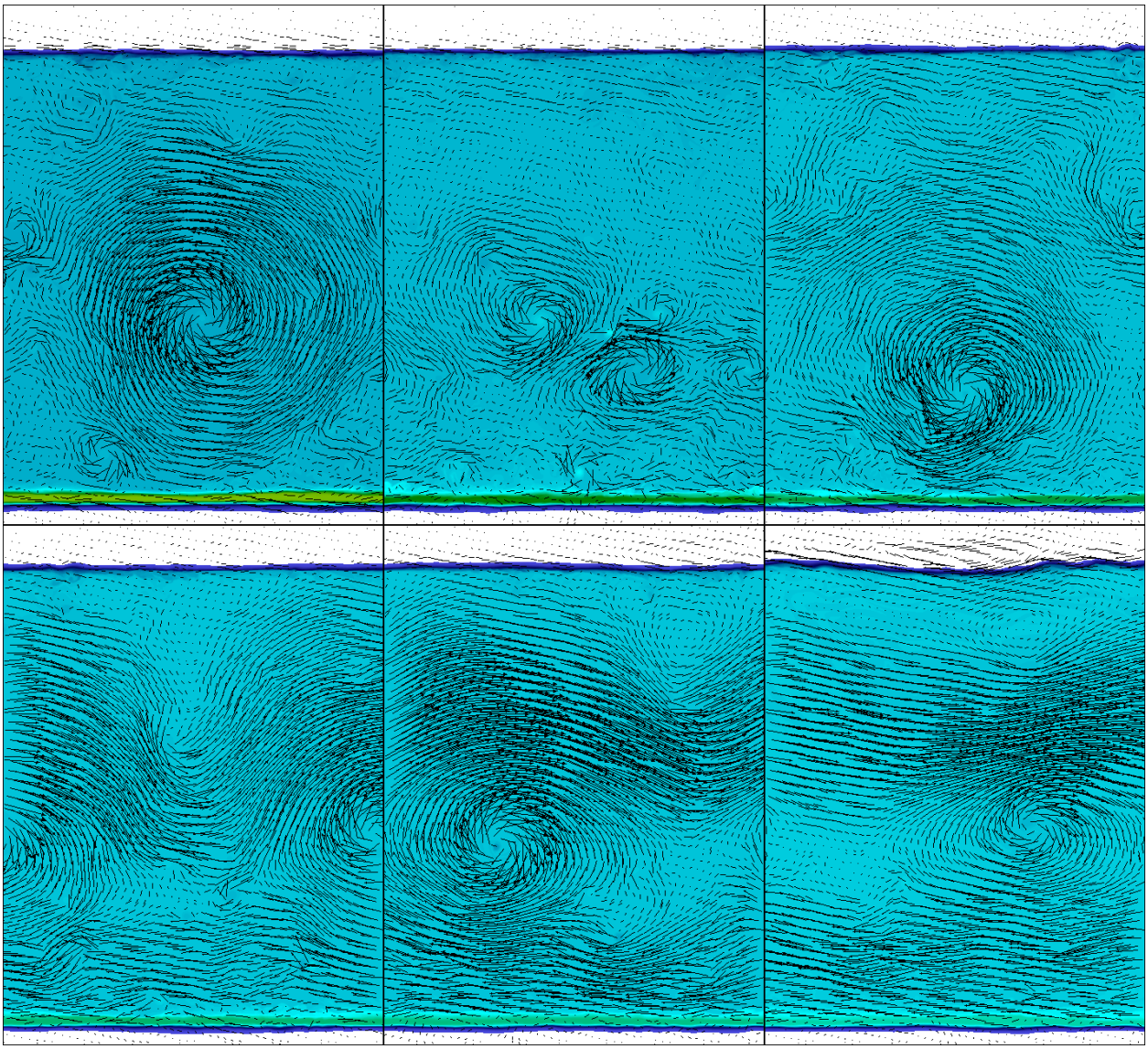

Fig. 13.— Colormap plot of ^{12}C mass fraction overplot with velocity vectors for the same region and times as shown in Figure 10.

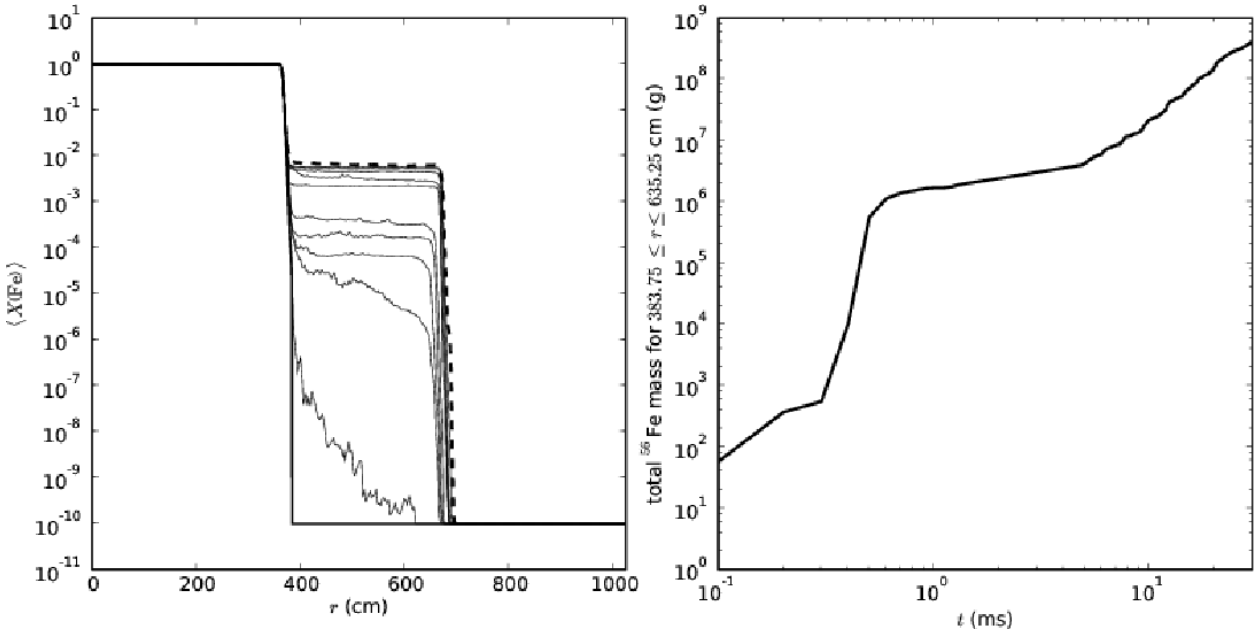

Fig. 14.— Plots showing the ^{56}Fe enrichment of the convective region. The left panel shows the evolution of the average ^{56}Fe mass fraction starting from the initial model distribution (solid thick line) and ending after 30 ms of evolution (dashed line). The right panel shows the total mass of ^{56}Fe in the convective region as a function of time.

REFERENCES

Alastuey, A., & Jancovici, B. 1978, ApJ, 226, 1034

Almgren, A. S., Bell, J. B., Nonaka, A., & Zingale, M. 2008, ApJ, 684, 449, paper III

Almgren, A. S., Bell, J. B., Rendleman, C. A., & Zingale, M. 2006a, ApJ, 637, 922, paper I

—. 2006b, ApJ, 649, 927, paper II

Altamirano, D., Watts, A., Linares, M., Markwardt, C. B., Strohmayer, T., & Patruno, A. 2010, ArXiv e-prints

Arnett, D., Meakin, C., Starrfield, S., Timmes, F., & Young, P. 2008, in American Institute of Physics Conference Series, Vol. 1001, Evolution and Nucleosynthesis in AGB Stars, ed. R. Guandalini, S. Palmerini, & M. Busso, 287–294

Arnett, W. D., Meakin, C., & Young, P. A. 2009, ArXiv e-prints 0910.0821

Bhattacharyya, S. 2010, ArXiv e-prints 1001.1642

Bildsten, L. 2000, in American Institute of Physics Conference Series, Vol. 522, American Institute of Physics Conference Series, ed. S. S. Holt & W. W. Zhang, 359–369

Böhm-Vitense, E. 1958, Zeitschrift fur Astrophysik, 46, 108

Caughlan, G. R., & Fowler, W. A. 1988, Atomic Data and Nuclear Data Tables, 40, 283, see also http://www.phy.ornl.gov/astrophysics/data/cf88/index.html

Cumming, A. 2003, ApJ, 595, 1077

Cumming, A., & Bildsten, L. 2000, ApJ, 544, 453

Fryxell, B. A., & Woosley, S. E. 1982, ApJ, 258, 733

Fushiki, I., & Lamb, D. Q. 1987, ApJ, 323, L55

Graboske, H. C., Dewitt, H. E., Grossman, A. S., & Cooper, M. S. 1973, ApJ, 181, 457

Heger, A., Cumming, A., Galloway, D. K., & Woosley, S. E. 2007, ApJ, 671, L141

Heger, A., Langer, N., & Woosley, S. E. 2000, ApJ, 528, 368

Lin, D. J., Bayliss, A., & Taam, R. E. 2006, ApJ, 653, 545

Muno, M. P., Chakrabarty, D., Galloway, D. K., & Psaltis, D. 2002, ApJ, 580, 1048

Narayan, R., & Cooper, R. L. 2007, ApJ, 665, 628

Nonaka, A., Almgren, A. S., Bell, J. B., Lijewski, M. J., Malone, C. M., & Zingale, M. 2010, ApJS, 188, 358, paper V

Pember, R. B., Howell, L. H., Bell, J. B., Colella, P., Crutchfield, C. Y., Fiveland, W. A., & Jessee, J. P. 1998, Combustion Science and Technology, 140, 123

Shara, M. M. 1982, ApJ, 261, 649

Spitkovsky, A., Levin, Y., & Ushomirsky, G. 2002, Astrophysical Journal, 566, 1018

Steiner, A. W., Lattimer, J. M., & Brown, E. F. 2010, ArXiv e-prints

Strohmayer, T., & Bildsten, L. 2006, Compact Stellar X-Ray Sources, ed. W. H. G. Lewin & M. van der Klis (Cambridge: Cambridge Univ. Press), 113–+

Strohmayer, T. E., Zhang, W., Swank, J. H., Smale, A., Titarchuk, L., Day, C., & Lee, U. 1996, ApJ, 469, L9+

Swesty, F. D., & Myra, E. S. 2009, ApJS, 181, 1

Taam, R. E., Woosley, S. E., Weaver, T. A., & Lamb, D. Q. 1993, ApJ, 413, 324

Timmes, F. X. 2000, ApJ, 528, 913

Timmes, F. X., & Swesty, F. D. 2000, ApJS, 126, 501

Weaver, T. A., Zimmerman, G. B., & Woosley, S. E. 1978, ApJ, 225, 1021

Woosley, S. E., & Weaver, T. A. 1984, in American Institute of Physics Conference Series, Vol. 115, American Institute of Physics Conference Series, ed. S. E. Woosley, 273–+

Zingale, M., Almgren, A. S., Bell, J. B., Nonaka, A., & Woosley, S. E. 2009, ApJ, 704, 196, paper IV

Zingale, M. et al. 2002, Astrophysical Journal Supplement, 143, 539

—. 2001, Astrophysical Journal Supplement, 133, 195

A. Changes Since Paper V

A.1. Thermal Diffusion

Here we describe the changes from Paper V due to the inclusion of the thermal conduction term in equation (3). Applying the chain rule to the EOS, $h = h(p_0, T, X)$, we note that the temperature gradient can be expressed as

$$\nabla T = \frac{1}{c_p}\nabla h + \sum_k \frac{\xi_k}{c_p}\nabla X_k + \frac{h_p}{c_p}\nabla p_0. \tag{A1}$$

In the edge state prediction, we compute the thermal conduction forcing term for temperature, as well as the thermal conduction term in S using h, X, and p_0 as inputs to the equation of state. We account for thermal diffusion in the cell update state immediately after both **Step 4** and **Step 8** in Paper V, as described below.

Step 4.1 *Diffuse the enthalpy through a time interval of* Δt.

Compute $k_{\rm th}^{(1)}, c_p^{(1)}$, and $\xi_k^{(1)}$ from $\rho^{(1)}, T^{(1)}$, and $X_k^{(1)}$ as inputs to the EOS. Note that density is constant in this step, i.e., $\rho^{(2'),\star} = \rho^{(2),\star}$. We also denote the result for enthalpy in **Step 4H** of Paper V as $(\rho h)^{(2'),*}$ rather than $(\rho h)^{(2),*}$ to indicate that we are about to account for thermal diffusion. The update is given by

$$\begin{aligned}(\rho h)^{(2),\star} &= (\rho h)^{(2'),\star} + \frac{\Delta t}{2}\nabla\cdot\left(\frac{k_{\rm th}^{(1)}}{c_p^{(1)}}\nabla h^{(2),\star} + \frac{k_{\rm th}^{(1)}}{c_p^{(1)}}\nabla h^{(1)}\right)\\ &\quad -\frac{\Delta t}{2}\sum_k \nabla\cdot\left(\frac{\xi_k^{(1)}k_{\rm th}^{(1)}}{c_p^{(1)}}\nabla X_k^{(2),\star} + \frac{\xi_k^{(1)}k_{\rm th}^{(1)}}{c_p^{(1)}}\nabla X_k^{(1)}\right)\\ &\quad -\frac{\Delta t}{2}\nabla\cdot\left(\frac{h_p^{(1)}k_{\rm th}^{(1)}}{c_p^{(1)}}\nabla p_0^{(2),\star} + \frac{h_p^{(1)}k_{\rm th}^{(1)}}{c_p^{(1)}}\nabla p_0^{(1)}\right),\end{aligned} \tag{A2}$$

which is numerically implemented as a diffusion equation for $h^{(2),\star}$,

$$\begin{aligned}\left(\rho^{(2),\star} - \frac{\Delta t}{2}\nabla\cdot\frac{k_{\rm th}^{(1)}}{c_p^{(1)}}\nabla\right)h^{(2),\star} &= (\rho h)^{(2'),\star} + \frac{\Delta t}{2}\nabla\cdot\frac{k_{\rm th}^{(1)}}{c_p^{(1)}}\nabla h^{(1)}\\ &\quad -\frac{\Delta t}{2}\sum_k \nabla\cdot\left(\frac{\xi_k^{(1)}k_{\rm th}^{(1)}}{c_p^{(1)}}\nabla X_k^{(2),\star} + \frac{\xi_k^{(1)}k_{\rm th}^{(1)}}{c_p^{(1)}}\nabla X_k^{(1)}\right)\\ &\quad -\frac{\Delta t}{2}\nabla\cdot\left(\frac{h_p^{(1)}k_{\rm th}^{(1)}}{c_p^{(1)}}\nabla p_0^{(2),\star} + \frac{h_p^{(1)}k_{\rm th}^{(1)}}{c_p^{(1)}}\nabla p_0^{(1)}\right),\end{aligned} \tag{A3}$$

$$T^{(2),\star} = T\left(\rho^{(2),\star}, h^{(2),\star}, X_k^{(2),\star}\right) \text{ using the EOS.} \tag{A4}$$

Step 8.1 *Diffuse the enthalpy through a time interval of* Δt.

Compute $k_{\rm th}^{(2),\star}, c_p^{(2),\star}$, and $\xi_k^{(2),\star}$, from $\rho^{(2),\star}, T^{(2),\star}$, and $X_k^{(2),\star}$ as inputs to the EOS. Note that density is constant in the diffusion step, i.e., $\rho^{(2')} = \rho^{(2)}$ We also denote the result for enthalpy in **Step 8H** of Paper V as $(\rho h)^{(2')}$ rather than $(\rho h)^{(2)}$ to indicate that we are about to account for thermal diffusion. The update is given by

$$\begin{aligned}(\rho h)^{(2)} &= (\rho h)^{(2')} + \frac{\Delta t}{2}\nabla\cdot\left(\frac{k_{\rm th}^{(2),\star}}{c_p^{(2),\star}}\nabla h^{(2)} + \frac{k_{\rm th}^{(1)}}{c_p^{(1)}}\nabla h^{(1)}\right)\\ &\quad -\frac{\Delta t}{2}\sum_k \nabla\cdot\left(\frac{\xi_k^{(2),\star}k_{\rm th}^{(2),\star}}{c_p^{(2),\star}}\nabla X_k^{(2)} + \frac{\xi_k^{(1)}k_{\rm th}^{(1)}}{c_p^{(1)}}\nabla X_k^{(1)}\right)\\ &\quad -\frac{\Delta t}{2}\nabla\cdot\left(\frac{h_p^{(2),\star}k_{\rm th}^{(2),\star}}{c_p^{(2),\star}}\nabla p_0^{(2)} + \frac{h_p^{(1)}k_{\rm th}^{(1)}}{c_p^{(1)}}\nabla p_0^{(1)}\right),\end{aligned} \tag{A5}$$

which is numerically implemented as a diffusion equation for $h^{(2)}$,

$$\begin{aligned}\left(\rho^{(2)} - \frac{\Delta t}{2}\nabla\cdot\frac{k_{\rm th}^{(2),\star}}{c_p^{(2),\star}}\nabla\right)h^{(2)} &= (\rho h)^{(2')} + \frac{\Delta t}{2}\nabla\cdot\frac{k_{\rm th}^{(1)}}{c_p^{(1)}}\nabla h^{(1)}\\ &\quad -\frac{\Delta t}{2}\sum_k \nabla\cdot\left(\frac{\xi_k^{(2),\star}k_{\rm th}^{(2),\star}}{c_p^{(2),\star}}\nabla X_k^{(2)} + \frac{\xi_k^{(1)}k_{\rm th}^{(1)}}{c_p^{(1)}}\nabla X_k^{(1)}\right)\\ &\quad -\frac{\Delta t}{2}\nabla\cdot\left(\frac{h_p^{(2),\star}k_{\rm th}^{(2),\star}}{c_p^{(2),\star}}\nabla p_0^{(2)} + \frac{h_p^{(1)}k_{\rm th}^{(1)}}{c_p^{(1)}}\nabla p_0^{(1)}\right),\end{aligned} \tag{A6}$$

$$T^{(2)} = T\left(\rho^{(2)}, h^{(2)}, X_k^{(2)}\right) \text{ using the EOS.} \tag{A7}$$

A.2. Volume Discrepancy Factor

We recall from Paper II, the full velocity field, $\boldsymbol{U}(\boldsymbol{x}, r, t)$, is decomposed into a radial component, $w_0(r,t)$, which governs the base state and an additional component, $\widetilde{\boldsymbol{U}}(\boldsymbol{x}, r, t)$, which governs the local dynamics:

$$\boldsymbol{U} = \widetilde{\boldsymbol{U}} + w_0\boldsymbol{e}_r. \tag{A8}$$

From (9) we then have

$$\frac{\partial\left(\beta_0 w_0\right)}{\partial r} + \nabla\cdot\left(\beta_0\widetilde{\boldsymbol{U}}\right) = \beta_0\left(S - \frac{1}{\overline{\Gamma}_1 p_0}\frac{\partial p_0}{\partial t} - \frac{f}{\overline{\Gamma}_1 p_0}\frac{p_0 - p_{\rm EOS}}{\Delta t}\right). \tag{A9}$$

Averaging (A9) as defined in (6) and recalling $\overline{\nabla \cdot \left(\beta_0 \widetilde{\boldsymbol{U}}\right)} = 0$, we have

$$\frac{\partial \left(\beta_0 w_0\right)}{\partial r} = \beta_0 \left(\overline{S} - \frac{1}{\overline{\Gamma}_1 p_0} \frac{\partial p_0}{\partial t} - \frac{f}{\overline{\Gamma}_1 p_0} \frac{p_0 - \overline{p_{\rm EOS}}}{\Delta t} \right). \tag{A10}$$

Subtracting (A10) from (A9) we have the divergence constaint on $\widetilde{\boldsymbol{U}}$:

$$\nabla \cdot \left(\beta_0 \widetilde{\boldsymbol{U}}\right) = \beta_0 \left(S - \overline{S} - \frac{f}{\overline{\Gamma}_1 p_0} \frac{\overline{p_{\rm EOS}} - p_{\rm EOS}}{\Delta t} \right). \tag{A11}$$

B. Test of the Diffusion Solver

This problem is designed to test the performance and accuracy of our implementation of an implicit solver for the diffusion of a two-dimensional Gaussian enthalpy pulse. That is, we are only concerned with the diffusive term in (3):

$$\frac{\partial(\rho h)}{\partial t} = \nabla \cdot \left(k_{\rm th} \nabla T\right). \tag{B1}$$

To easily compare with an analytic solution (see Swesty & Myra (2009) and references therein for an analogous example for a radiation-hydrodynamics code) we assume the thermal conductivity to be constant: $k_{\rm th} = 10^7$ erg K cm^{-1} s^{-1}. We assume an ideal gas with $X(\mathrm{He}^4) = 0.5, X(\mathrm{C}^{12}) = X(\mathrm{Fe}^{56}) = 0.25$ and ratio of specific heats $\gamma = 5/3$. Furthermore, we are not concerned with any hydrodynamic motions so we keep the density fixed. We can then express (B1) in a more customary form:

$$\frac{\partial h}{\partial t} = D \nabla^2 h, \tag{B2}$$

where $D = k_{\rm th} / \left(\rho c_p\right)$ is the diffusion coefficient.

Given the initial conditions for the two-dimensional pulse,

$$h(\mathbf{r}, t = t_0) = \left(h_{\rm p} - h_0\right) \times \exp\left(\frac{-\left|\mathbf{r} - \mathbf{r_0}\right|^2}{4 D t_0} \right) + h_0, \tag{B3}$$

where h_p, h_0, $\mathbf{r_0}$, and t_0 are the peak enthalpy, background enthalpy, location of the center of the peak and time from which the system has evolved respectively, the analytic solution takes on the form

$$h(\mathbf{r}, t) = \left(h_{\rm p} - h_0\right) \left(\frac{t_0}{t + t_0} \right) \exp\left(\frac{-\left|\mathbf{r} - \mathbf{r_0}\right|^2}{4 D \left(t + t_0\right)} \right) + h_0, \tag{B4}$$

where t is the evolved time.

We solve this problem on a Cartesian grid of size 2 cm × 2 cm with the following parameters: $h_{\rm p} = 10.0$ erg g^{-1}, $h_0 = 1.0$ erg g^{-1}, $\mathbf{r_0} = (1.0\text{ cm}, 1.0\text{ cm})$, $t_0 = 0.1$ s, and $\rho = 1.0$ g cm^{-3}. For the density and composition used in this test, we obtain a diffusion coefficient of $D = 0.32$ cm^2 s^{-1}. The timestep size for our implicit scheme is given by

$$\Delta t = \alpha \Delta t_{\rm explicit},$$

where $\Delta t_{\rm explicit}$ is an approximation to the explicit timestep restriction,

$$\Delta t_{\rm explicit} \sim \frac{\Delta x^2}{D},$$

where Δx is the grid spacing of our uniform grid and α is a constant. Figure 15 shows an example of the initial pulse and its evolution through $t = 0.06s$ with $\alpha = 1$. Figure 16 shows the average enthalpy as a function of radius compared to the analytic solution for the same test problem shown in Figure 15. Excepting boundary effects, the numerical and analytic solutions are well matched. We evaluated the problem with several different values of α and compared the results to the analytic solution at any given timestep by calculating the Euclidean residual defined by

$$R_\alpha = \left(\frac{\sum_i \left(h(r_i) - h_{\alpha,i} \right)^2}{\sum_i h(r_i)^2} \right)^{1/2},$$

where $h(r_i)$ represents the *analytic solution* as given by (B4) evaluated at radial grid point r_i and $h_{\alpha,i}$ represents the *numerical solution* for the average enthalpy at that grid point for a particular value of α. Figure 17 shows the value of R_α for three different values of α as a function of time. Also plotted is the ratio R_α / R_1 for $\alpha = 10, 100$ to show the error introduced when taking a larger timestep size to reach the same simulation time, t. In this example, the maximum percent difference in residual between the solution at the explicit timestep size ($\alpha = 1$) and those with larger timestep size is $\lesssim 2.5\%$.

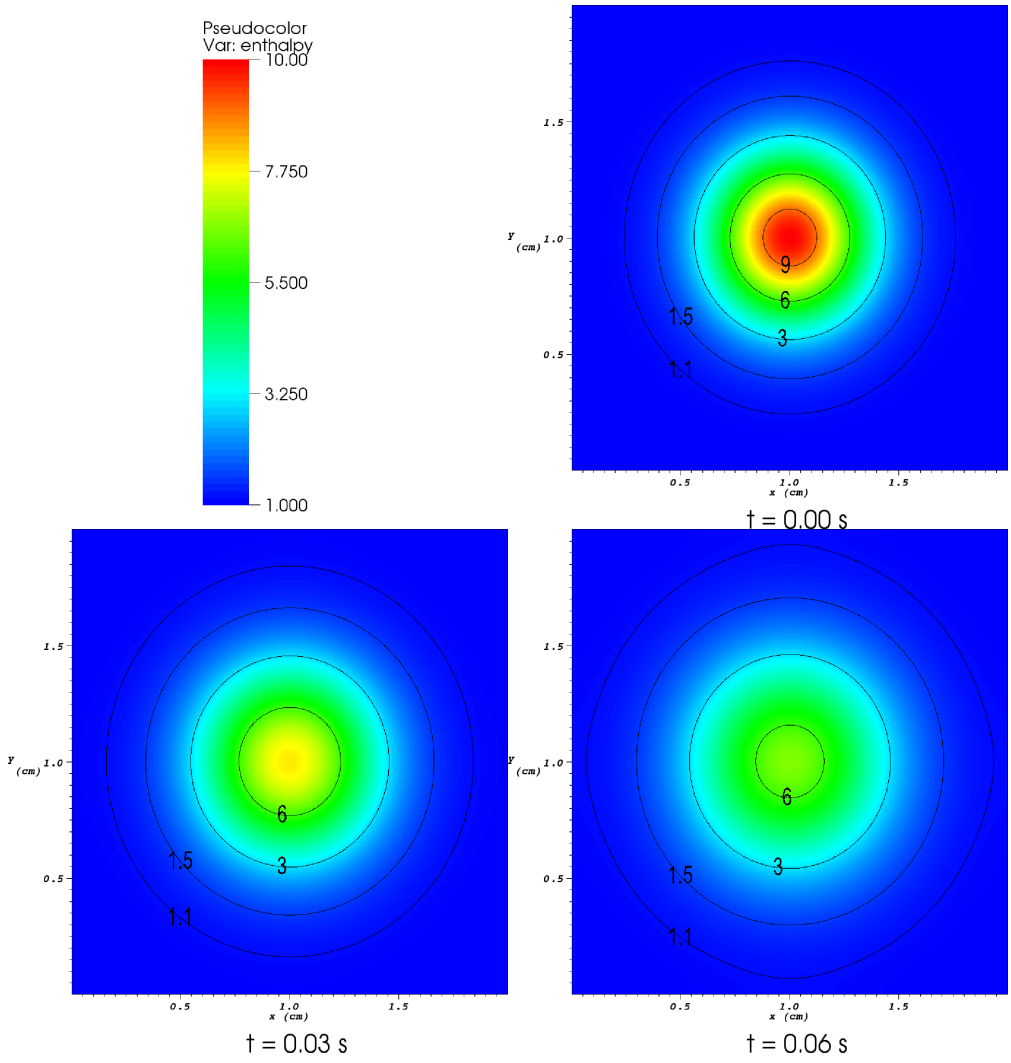

Fig. 15.— Time evolution of the diffusion of a two-dimensional Gaussian pulse of enthalpy as described in the text. The value of time displayed is the evolution time, t. This simulation was run with a value of $\alpha = 1$ - i.e. with timestep size equal to the explicit timestep. Excepting edge effects near the domain boundary, the numerical solution maintains its axisymmetric form about the center of the pulse at $(x, y) = (1.0, 1.0)$.

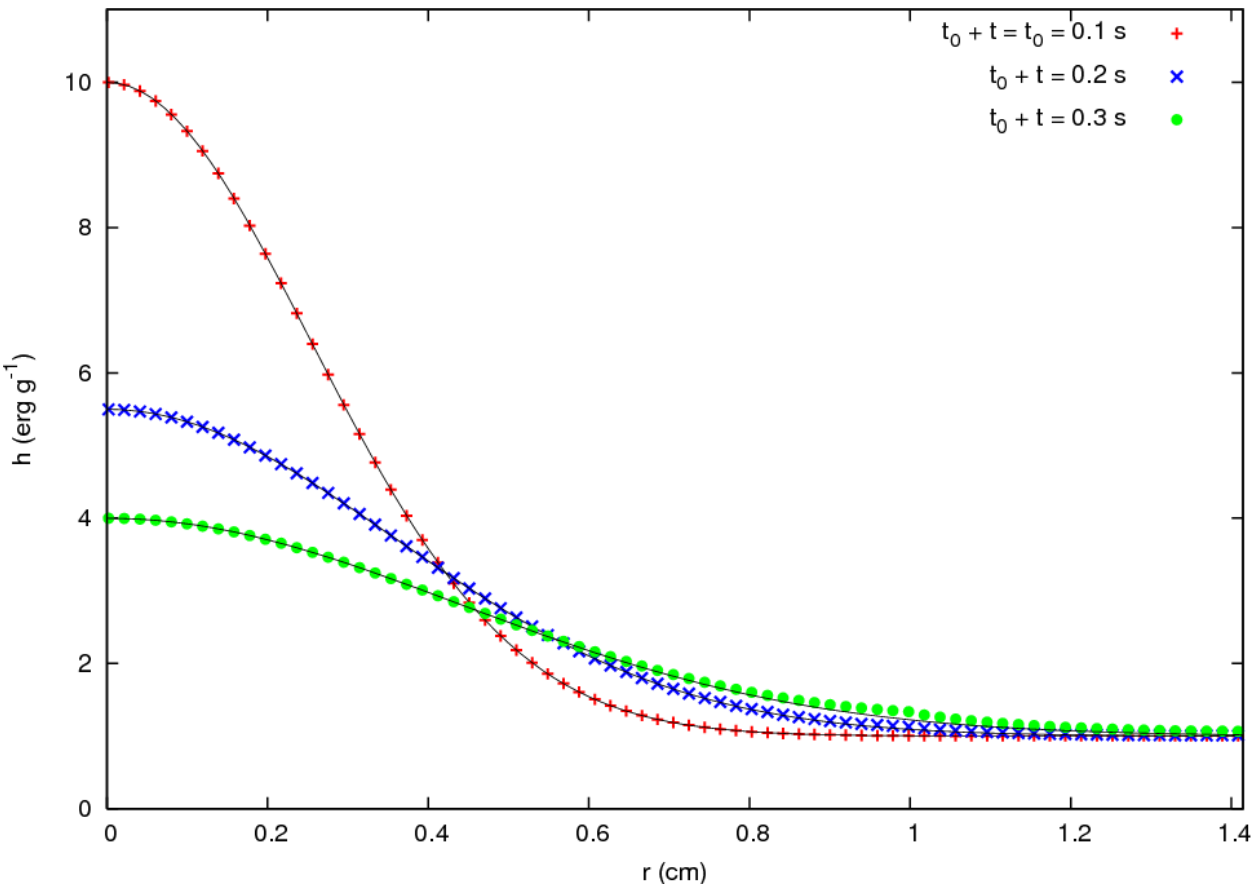

Fig. 16.— The average of enthalpy as a function of radius from the center, $(x, y) = (1.0, 1.0)$, of a two-dimensional Gaussian pulse. The crosses, X's and circles are data from the numerical solution at the shown times. The black lines represent the analytic solutions as given by (B4). The numerical solution tracks the analytic solution very well except when the pulse has diffused enough that it begins to interact with the boundaries of the computational domain.

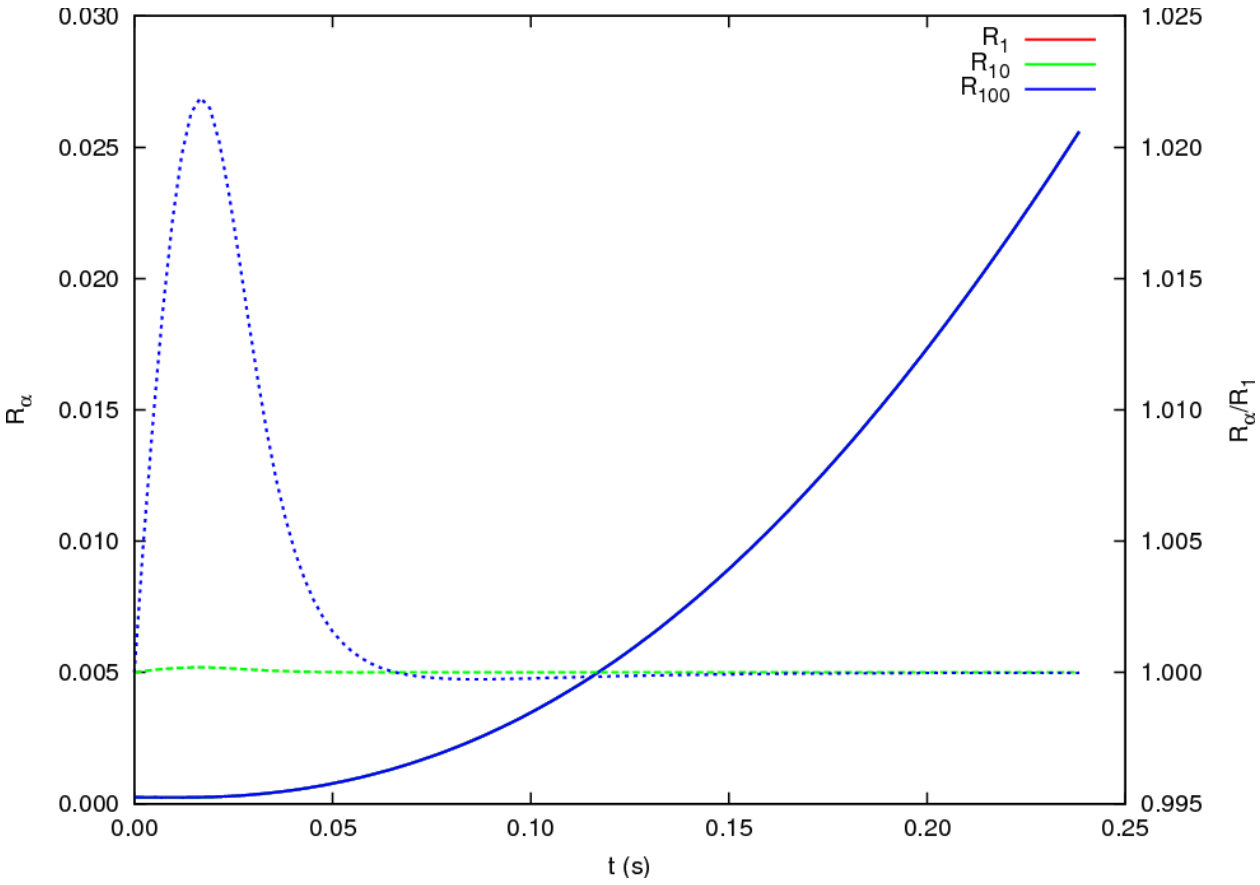

Fig. 17.— Comparison of accuracy of the numerical scheme for 3 different values of α. The solid lines correspond to R_α for the given values of α and all overlap. The dashed lines correspond to the ratio of R_α/R_1 to help elucidate the increase in residual when taking a larger timestep.